RESEARCH ARTICLE

WILEY

Probabilistic seismic performance assessment of steel moment-resisting frames considering exposed column-base plate connections with ductile anchor rods

Biao Song[1,2] | Ahmad Hassan[3,4] (ID) | Amit Kanvinde[3] | Carmine Galasso[2,5] (ID)

[1]Civil Engineering Institute, École Polytechnique Fédérale de Lausanne (EPFL), Lausanne, Switzerland

[2]Department of Civil, Environmental & Geomatic Engineering, University College London, London, UK

[3]Department of Civil and Environmental Engineering, University of California, Davis, California, USA

[4]Degenkolb Engineers, Sacramento, California, USA

[5]Scuola Universitaria Superiore (IUSS) Pavia, Pavia, Italy

Correspondence
Carmine Galasso, Department of Civil Environmental and Geomatic Engineering, University College London United Kingdom of Great Britain and Northern Ireland, London WC1E 6BT, United Kingdom of Great Britain and Northern, Ireland.
Email: c.galasso@ucl.ac.uk

Abstract

This paper presents a numerical study assessing the seismic performance of steel moment-resisting frames (SMRFs) designed with ductile exposed column-base plate (ECBP) connections employing yielding anchor rods. For their potential use as weak bases, the proposed ECBP detail is designed to accommodate plastic deformations in the anchors. The seismic performance of 2- and 4-story archetype SMRFs with ECBPs is investigated to examine the effects of various base-connection strengths on the frame collapse mechanisms and probabilities. To this aim, the ECBP connections of each frame are designed for a set of three strength levels, ranging from reduced seismic loads to capacity-designed forces of the adjoining columns. These designs enable the base responses to vary from highly inelastic (i.e., weak-base design) to elastic (i.e., strong-base design) when subjected to earthquake-induced ground shaking. Nonlinear time history analysis (NLTHA) is extensively performed, applying a suite of assembled ground-motion sequences (i.e., two ground motions in series) to assess the ECBP connection response and the corresponding frame behavior. Fragility analyses accounting for only the first ground motions in each considered sequence (to derive fragility curves), and the entire ground-motion sequences (to derive fragility surfaces) are also performed to evaluate the probabilities of frame collapse and base connection failure. Finally, key findings regarding the seismic performance of ductile ECBP connections and their effects on the frame collapse are discussed. The limitations of the study are also outlined.

KEYWORDS
ductile column-base connection, fragility assessment, seismic performance, steel moment-resisting frame

Novelty

- Novel simulation-based study to explicitly assess the seismic performance of low- to mid-rise steel moment-resisting frames (SMRFs) designed with ductile exposed column-base plate (ECBP) connections proposed by the authors.
- 2- and 4-story archetype SMRFs designed for a high-seismicity location in California; and for each SMRF, ECBP connections designed for three distinct strength levels to examine the effects of various base connection strengths on the frame collapse mechanisms and probabilities.
- Fragility models of frame collapse and ECBP connection failure, including fragility curves for single ground motions and fragility surfaces for ground motion sequences, derived for the archetype SMRFs designed with different base strength levels.
- Results indicate that the SMRFs designed with weak ECBP connections may also exhibit acceptable seismic performance compared to strong-base SMRFs. This may result in impactful and practical changes to the seismic design of weak-base steel frames.

1 | INTRODUCTION AND MOTIVATION

On the west coast of the United States (US) and elsewhere, steel moment-resisting frames (SMRFs) are a widely used lateral-force-resisting system for earthquake loadings. To achieve an overall ductile structural behavior under lateral loadings, SMRFs are typically designed to concentrate yielding in plastic hinges at beam ends over the entire height of the frames. The other structural components (e.g., columns, panel zones, and connections), which are presumed to have limited ductility, are usually designed to remain elastic (e.g., the American Institute of Steel Construction's AISC 341-16[1]). This is accomplished by designing these components for overstrength seismic forces considering a system-specific overstrength factor (Ω) and/or by capacity-design criteria (i.e., designing the component to resist the expected strain-hardened strength of the connected elements). Following these design concepts, undesirable soft stories may be avoided, and an overall ductile structural behavior can be achieved. From the kinematics standpoint, plastic hinges are also expected at the bases of the first-story columns to achieve a full-building sidesway mechanism. These plastic hinges may be formed either in the bottom region of the steel columns or in the column-base connections/foundations.

In the case of low- to mid-rise SMRFs, exposed column-base plate (ECBP) connections are commonly used to transfer seismic forces (e.g., flexural, axial, and shear forces) from the superstructure to the supporting foundation. Currently, the dominant design practice is to make ECBP connections flexurally stronger than the corresponding base columns (i.e., strong-base design—forcing the plastic hinges into the bottom ends of the columns). This choice is made because (1) base connections are supposedto be brittle compared to the rolled steel column sections; and (2) the flexural inelastic response of steel columns is better understood and quantified. Following this design option, ECBP connections are usually required to withstand the fully yielded and strain-hardened moment (= $1.1R_yM_p$, where R_y is the ratio between the expected and nominal yield stresses of steel material, and M_p is the plastic moment) of the connected column combined with the overstrength axial force. Designing ECBP connections through this approach is costly, usually resulting in thick plates and multiple large anchor rods.[2] Moreover, recent experimental[3–6] and numerical[7–9] studies on the seismic performance of ECBP connections reveal their high rotation capacities (> 5%). These capacities are achieved even without any explicit detailing for ductility. It is also noticed that ECBP rotation capacities may be comparable to the rotation capacities of wide-flanged columns due to local and lateral instabilities. This is especially the case when the columns are subjected to the combination of axial and cyclic inelastic flexural loadings.[10–12] These findings suggest that the strong-base design approach may also be unnecessary. As a result, a weak-base design approach may be adopted, accommodating inelastic deformations in the ductile base connections. This is also permitted by AISC 341-16[1] *Section D2.6c*, using overstrength seismic loads to design ECBP connections provided that "*a ductile limit state in either the column-base or the foundation controls the design.*" However, ductile ECBP connections are not commonly adopted because (1) the economical and convenient detailing for ductile ECBP connections and the associated failure modes have not been widely investigated; (2) there are no prescriptive guidelines for the seismic design of ductile ECBP details; and (3) the effects of the ductile response of ECBP connections on the global performance of SMRFs (e.g., collapse probability) are not well understood.
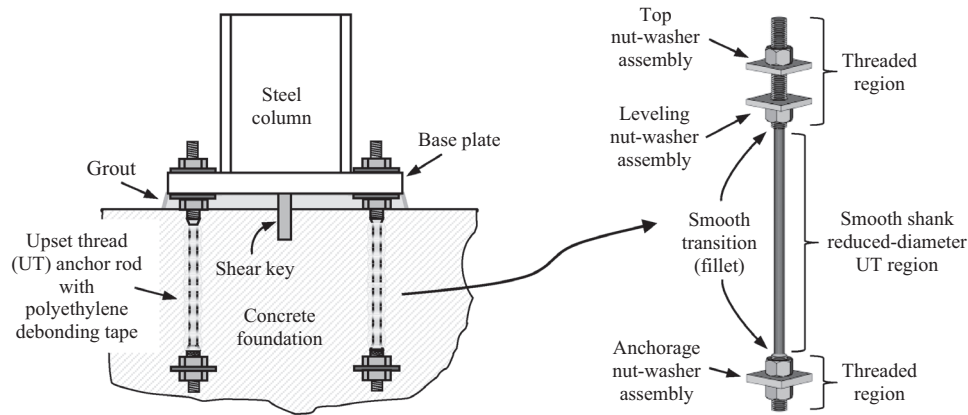
FIGURE 1 Schematic illustration of the proposed ductile ECBP connection with UT anchor rod details.

Attempting to partially address these issues above, particularly the first one, Hassan et al.[13] developed a highly ductile ECBP detail with yielding anchors (see Figure 1). This detail features upset thread (UT) anchor rods with a smooth shank to accommodate cyclic inelastic deformations while the steel base plate remains elastic. The shank is frictionally isolated from the concrete foundation using polyethylene debonding tape. In that study, the cyclic response of the proposed ECBP detail was investigated through four full-scale experimental tests and a large set of complementary simulations. Two possible failure modes were also identified: (1) necking of the anchors in the UT region, leading to strain accumulation and fracture; and (2) ultra-low cycle fatigue (ULCF) fracture of the anchors due to plastic strains accumulated homogenously over the UT length. Findings from the study indicated that the proposed ECBP detail is promising and can provide significant ductility given high seismic demands. However, this study only focused on the connection response, and its interactions with SMRFs were not considered.

Against this backdrop, the present study further examines the strength of the proposed ductile ECBP connections and the resulting structural performance of two case-study frames to establish a quantitative context within which design strategies for ductile ECBPs in SMRFs may be further developed. Specifically, this study conducts a large set of nonlinear time history analyses (NLTHAs) of 2- and 4-story archetype SMRFs designed as per the current design standards in the US (i.e., American Society of Civil Engineers' ASCE 7–10[14] and AISC 341-16[1]) and employing the proposed ECBP detailing. Cloud-based NLTHAs[15] and seismic fragility analysis are performed to investigate the effects of various base strengths on the ECBP connection and global (frame) performance within the designed SMRFs. In particular, the considered strengths vary from a low value (i.e., designing ductile ECBP connections for the reduced seismic loads with a response modification coefficient, $R = 8$[14]) to a high value (i.e., designing ECBP connections for $1.1R_y M_p$ of the connected column). Following this, a wide range of ECBP connection responses (from elastic to highly inelastic) are examined. To appropriately interpret the cloud-based NLTHA and fragility results per code-based design practice,[14] 5%-damped (pseudo-) spectral acceleration at the code-based (rather than the actual) fundamental period of the frame, $S_a(T_1)$ is selected as the ground-motion intensity measure (IM) in the study. It is noticed that the code-based T_1 has an upper limit[14] and is usually lower than the actual T_1 of the archetype frames assessed in this study.[16] This implies that the $S_a(T_1)$ value at the code-based period is higher, which may be considered more critical when, for instance, estimating the frame collapse probability at the specific spectral acceleration levels. According to Hassan et al.,[13] the proposed ductile ECBP connection may experience cumulative damage due to ULCF in the anchor UT region, eventually leading to base connection failure (BCF). To properly investigate the damage cumulation, a suite of 800 ground-motion sequences (GMSs), each combining two ground motions (herein called GM1 and GM2, for the first and second ground motions in a GMS, respectively), are assembled for NLTHAs of each archetype SMRF. Accordingly, fragility curves and surfaces for BCF and collapse probabilities can be derived, considering GM1s only and GMSs, respectively.

This paper begins by summarizing the methodological components set for NLTHAs in Section 2. This section briefly describes the design and modeling strategies of the two archetype SMRFs, the proposed ductile ECBP connections, and the GMS selection. The following section (Section 3) presents the failure criteria for the seismic performance assessment of SMRFs; the results of simulations are discussed with an emphasis on characterizing the effects of ECBP strength on the failure mechanisms of SMRFs. Then, fragility analysis is performed in Section 4, providing fragility curves and surfaces
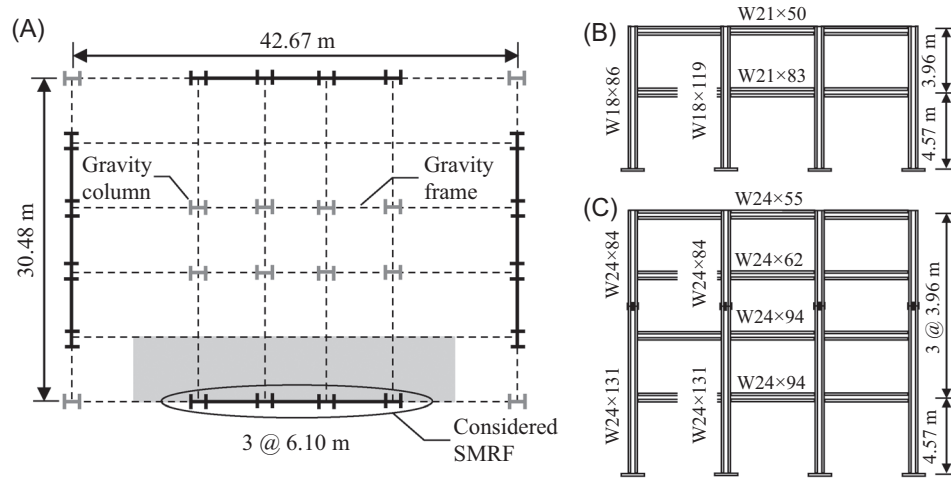
FIGURE 2 Schematic illustration of archetype frames: (A) plan configuration; (B) 2-story elevation view; and (C) 4-story elevation view.

for archetype SMRFs with ductile ECBP connections designed for different strength levels. Associated results and their implications for the design of ductile ECBP connections are also discussed. Finally, Section 5 summarizes the findings and limitations of the study.

2 | ARCHETYPE FRAMES AND GROUND-MOTION SEQUENCES

2.1 | Design of archetype SMRFs and ductile ECBP connections

Figure 2 schematically illustrates the dimensions and floorplan of the two archetype moment frames considered in this study. The 2-story (total height = 8.53 m) and 4-story (total height = 16.45 m) SMRFs are selected as archetype frames because taller frames generally rely on embedded-type base connections (e.g., see Grilli et al.[17]). The considered two buildings share the same floorplan[18] but a different number of stories because the building height is expected to be the most influential variable on the frame seismic performance, according to past research.[19–21] As shown in Figure 2, each of the two assessed SMRFs has three bays (6.10 m each) and is located at the perimeter of the building plan. In the design process, these SMRFs are assumed to resist half of the total seismic loading (of the entire buildings) but only receive the gravity loads of the tributary area (indicated as the shaded portion in Figure 2A). Member sizes (also given in Figure 2) are designed based on the following specific considerations:

- Beams and columns are designed with the ASTM (American Society for Testing and Materials) A992 steel[22] (specified minimum yield stress, $F_y = 345$ MPa; and specified minimum tensile strength, $F_u = 450$ MPa).
- The dead load of 4.31 kN/m^2 is uniformly distributed over each floor; a cladding load of 1.20 kN/m^2 is applied as a perimeter load; the unreduced live load is 2.39 kN/m^2 on all floors and 0.96 kN/m^2 on the roof.
- Seismic load and design checks as per ASCE 7–10[14] and AISC 341-16[1] are considered; wind loads are not considered because seismic loadings govern the lateral design forces.
- The archetype SMRFs are assumed to be located in downtown San Jose, California (a non-near-fault location; site class D conditions under the seismic design category D and risk category II; coordinates: 37.3°N, 121.9°W). The code-based fundamental periods (T_1) of the 2- and 4-story frames are 0.56 s and 0.95 s, respectively. These correspond to 5%-damped design basis earthquake (DBE, i.e., 10% probability of exceedance in 50 years, or 10/50 hazard) spectral acceleration (denoted $S_a(T_1)_{\mathrm{DBE}}$) values of 1.0 g and 0.63 g for the two frames. Corresponding 5%-damped spectral acceleration values at maximum considered earthquake (MCE, i.e., 2% probability of exceedance in 50 years, or 2/50 hazard) level (denoted $S_a(T_1)_{\mathrm{MCE}}$) are 1.5 g and 0.94 g, respectively.
- All the beams feature reduced beam section (RBS) connections (designed as per AISC 358-16[23]) to concentrate the inelastic rotations. Regarding the dimensions of all the RBS connections, the horizontal distance from the column flange face to the start of an RBS cut is assumed as 0.625 times the beam flange width; the length of the RBS cut and

the depth of cut at the center of the RBS are taken as 0.75 times the beam depth and 0.25 times the beam flange width, respectively.

- The shear design of joint panel zones is based on AISC 360-16[24] and AISC 341-16,[1] accounting for the effects of inelastic panel-zone deformation on SMRF stability.
- Both SMRFs are designed with a fixed-base assumption (following current practice). This implies that the effect of base flexibility on the building period is not considered, and the strong-column-weak-beam (SCWB) check for the first-story column design presumes an inflection point at the midspan of the column.

Additionally, key aspects of the design for the proposed ductile ECBP connection include:

- The concrete foundation design assumes a nominal concrete compressive strength of $f_c' = 27.58$ MPa and a concrete confinement factor of 2.0.[25]
- The base plates and anchor rods are designed with ASTM A572 Gr.50 steel[26] ($F_y = 345$ MPa) and ASTM F1554 Gr.105 steel[27] ($F_y = 724$ MPa and $F_u = 862$ MPa), respectively. The use of Gr.105 steel can largely reduce the number and size of designed anchor rods.
- Three distinct design strength levels for ductile ECBP connections are considered for each frame. These include the combinations of $(R, \Omega) = (8, 1)$; $(8, 3)$ for the design flexural and axial forces at the connection level and a case in which the base connection is designed for a moment of $1.1R_yM_p$. These are denoted by $R = 8$; $\Omega = 3$; and $1.1R_yM_p$, respectively. For each of these levels, the interior and exterior ECBP connections are designed for the following force demands: (1) the reduced seismic loads ($R = 8$ design case), that is, the axial force and moment corresponding to the design base shear and reduced by the R-factor[14] ($R = 8$), without the amplification due to system overstrength ($\Omega = 1$)—the latter generally implies the weak-base design of the ECBP connections; (2) the code-based overstrength seismic loads ($\Omega = 3$ design case),[14] that is, seismic forces corresponding to multiplication between Ω-factor ($= 3$) and the $R = 8$ cases; and (3) capacity designed forces ($1.1R_yM_p$ design case), that is, a design moment equals to $1.1R_yM_p$ of the connected column, with the overstrength axial force (i.e., same as $\Omega = 3$ design case); this is conventionally used for strong-base design. As such, these designs lead to a range of ECBP strengths and allow examining prospective design alternatives. In the $R = 8$ and $\Omega = 3$ cases (i.e., using base shear to determine the design base loadings), the ECBP connections are designed according to the equivalent lateral force analysis[14] with a fixed base assumption. This is consistent with current design practice for determining seismic loads in other elements of the SMRFs.
- The base plate and anchor UT region sizes of the ECBP connections are first designed as per the current design approach in the US (i.e., AISC *Design Guide One*[28]), with two exceptions. First, when determining the required thickness of the base plate, only the plate yielding check of the tension side of the connection is performed. The plate yielding check on the compression side is neglected because the overall base connection failure (in general) does not occur under this failure mode.[1,3] Second, the factor of 0.75 (to account for the reduction of the threaded area of an anchor) is omitted in the calculation of the nominal tensile strength of an anchor rod because the proposed ECBP connections feature smooth shank in their UT regions (see Figure 1).
- To achieve the expected ductile response of the ECBP connections (i.e., forcing inelastic deformations into anchor UT regions while keeping the base plate response elastic), three additional design considerations are made: (1) the diameters of the top and bottom threaded regions of the anchor rods are 6.35 mm larger than the corresponding UT diameters[13] (see Figure 1); (2) for safety purpose, the stretch length of the UT region is assumed as half of the base plate length, according to the findings of Hassan et al.[13]; and (3) the base plate thickness is further increased to confirm that the anchor rod failure is reached before the yielding failure of the base plate on the tension side of the connection. The last design check is accomplished by adopting the moment-axial force interaction curves (for the two considered failure modes) discussed in Gomez.[29] An example of such interaction curves is shown in Figure 3 for the strength level $R = 8$ of the 4-story frame. According to Figure 3A,B, for both exterior and interior base connections, the moment capacities corresponding to the base plate yielding on the tension side ($M_{cap,plate}$) are much larger than the flexural strengths due to anchor rod failure ($M_{cap,rod}$). In this study, the ratio of $M_{cap,rod}$ to $M_{cap,plate}$ at the design axial force level is designed to be about or less than 0.9 (see Table 1). Each panel illustrates two design points (i.e., design axial compression, P_{design}, and moment, M_{design}, loading pairs) of the exterior or interior connections in the 4-story frame (see Figure 2C). The loading pairs relating to the minimum compressive axial forces are observed to e closer to the interaction curves, so they control the design of ECBP connections. This finding is also reported by Torres-Rodas et al.[30]
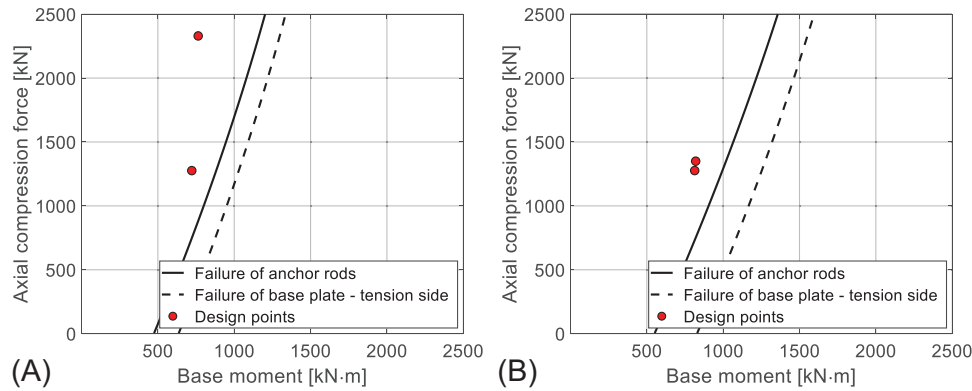
FIGURE 3 Moment-axial force interaction curves for 4-stroy frame with ECBP connections designed for R = 8 strength level: (A) exterior bases; and (B) interior bases.

TABLE 1 Critical design loading pairs, base strengths, and strong-base-plate-weak-rod checks of ductile ECBP connections.

Frame	Strength level	Exterior ECBP connection				Interior ECBP connection			
		P_{design} (kN)	M_{design} (kN m)	$M_{\text{cap,rod}}$ (kN m)	$\dfrac{M_{\text{cap,rod}}}{M_{\text{cap,plate}}}$	P_{design} (kN)	M_{design} (kN m)	$M_{\text{cap,rod}}$ (kN m)	$\dfrac{M_{\text{cap,rod}}}{M_{\text{cap,plate}}}$
2-story	$R = 8$	675	416	529	0.87	623	646	882	0.92
	$\Omega = 3$	300	1283	1838	0.88	600	1946	2690	0.88
	$1.1R_y M_p$	300	1271	1838	0.88	600	1791	2525	0.86
4-story	$R = 8$	1276	722	882	0.86	1276	814	995	0.79
	$\Omega = 3$	222	2208	3106	0.89	1203	2447	3283	0.92
	$1.1R_y M_p$	222	2529	3528	0.90	1203	2529	3473	0.90

Table 1 summarizes the critical design loading pair (as discussed above), the calculated base strength (i.e., $M_{\text{cap,rod}}$ at the design axial force level), and the $M_{\text{cap,rod}}/M_{\text{cap,plate}}$ ratio of each designed ECBP connection in the two considered archetype SMRFs. According to Table 1, the ratios of base-connection design moments (M_{design}) to moment strengths ($M_{\text{cap,rod}}$) vary between 0.69 and 0.82. This is mainly because a resistance factor of 0.75 is used to determine the number and diameter of anchor rods, as per AISC *Design Guide One*.[28]

2.2 | Simulation of SMRFs and ductile ECBP connections

Figure 4 schematically illustrates key aspects of the assembled SMRF nonlinear models with line-element-based (LEB) ECBP connection models in OpenSees.[31]

Steel beams and columns are simulated as elastic beam-column elements with zero-length rotational springs at the expected yielding locations (i.e., locations of RBS in the beams and ends of columns). The rotational constitutive response of these springs is simulated using the Ibarra-Medina-Krawinkler (IMK) deterioration model.[32] The IMK model parameter sets for beams with RBS and columns are calibrated based on the modeling recommendations by Lignos and Krawinkler[33] and Lignos et al.,[34] respectively. Beam-to-column joint panel zones are explicitly simulated by an assemblage of pin-connected rigid links in which one of the connections features a rotational spring, that is, the rotational-spring parallelogram.[35] The properties of the spring are calibrated to represent expected panel zone behaviors through a bilinear hysteretic model, as discussed by Gupta and Krawinkler.[36] A leaning column (to support appropriate gravity loads) is also modeled along with large-displacement geometric transformations to account for the P-Δ effects that induce frame sidesway collapse.

The details of ECBP connection model in OpenSees are also shown schematically in Figure 4. Instead of using point-hinge hysteretic models[37] for ECBP connections in frames,[7,9] this study selected the LEB model recently developed by Hassan et al.[13] In fact, this model can explicitly simulate the axial force–moment interaction and axial force variation during seismic loading, which are usually important for ECBP connections in SMRFs due to dynamic overturning effects.[8]
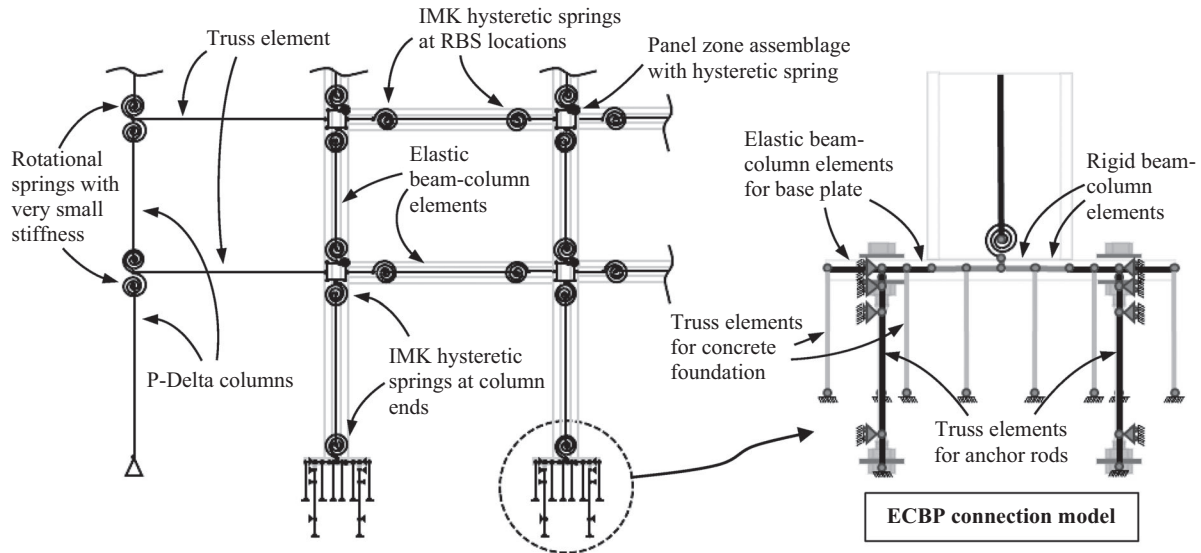
FIGURE 4 Key features of SMRF and ECBP connection models.

Also, the selected model can facilitate the investigation of BCF through the simulated base connection components; details of this aspect are discussed subsequently in Section 3.1. According to Figure 4, the base connection is represented by an assembly of uniaxial spring and beam-column elements: (1) the base plate is modeled by a set of beam-column elements—fiber cross-sections (considering the entire width of the plate) are assigned for the plate in the flap region outside the column depth, and elastic beam-column elements (modeled as rigid) are used to represent plate within the column depth; (2) the bearing response of the concrete foundation is modeled by 20 uniaxial truss elements (i.e., Winkler springs, not all shown in Figure 4 for simplicity) with zero tensile strength using Kent–Scott–Park concrete material model,[38,39] each representing the response of a segment of the concrete footing; and (3) anchor rods on each side of the connection are modeled as an assembly of three springs (i.e., uniaxial truss elements) in series. The center spring represents the UT section, and the two outer springs represent the anchor's top and bottom threaded regions. The constitutive response of the rod steel material is represented through the IMK model with a cap. This cap corresponds to the initiation of necking failure in the anchor rod, and a steep softening (i.e., post-capping behavior) is assigned to simulate the complete loss of tensile strength (i.e., fracture). The definition of anchor necking initiation in this study is discussed subsequently in Section 3.1. The parameters of all the material models used are calibrated through the relevant experiments.[13] In addition, lateral supports are provided for the nodes of each anchor segment. This implies that (1) the anchors in the LEB model are assumed to undergo purely axial deformations, and the bending in the UT regions may be negligible; and (2) the base shear is assumed to be transferred independently (e.g., using a shear key[40]). Validation of the LEB model for the proposed ECBP connection has been carried out by Hassan et al.[13] via four full-scale experiments. In this study, LEB models were constructed with the same configurations as the experimental specimens. These models were then subjected to the identical loading protocols as applied in the experiments. Overall, good agreement was found in the cyclic moment-rotation responses (including peak moment values, hysteretic behavior, and transition points associated with contact and gapping among connection components) between simulations and experimental results. Moreover, the vertical deformations of anchor rods obtained from simulations and experiments were close (showing a difference of less than 7%). The latter validation is important because it indicates that the LEB model is able to accurately predict the anchor rod elongation, and this elongation is a director indicator for the damage estimation of the ECBP connections (see Section 3). Details of the validation can be found in Hassan et al.[13]

2.3 | Selection and assembly of ground-motion sequences

One of the objectives of this study is to investigate the effects of single and/or multiple earthquake-induced ground motions and the resulting damage accumulation on the failure probability of ductile ECBP connections and the collapse probability of SMRFs. To this aim, a large number of GMSs are used in this study to perform cloud-based NLTHAs. Specifically,

each considered GMS consists of a pair of ground motions (i.e., GM1 and GM2). This choice may be justified through the Markovian assumption[41]—the damage increment in one event/ground motion (e.g., GM2) depends on the previous seismic history only via the state of the structure at the time the seismic event occurs (i.e., after GM1). Some past studies adopted real (i.e., recorded) mainshock-aftershock (MS-AS) sequences to represent sequences of GM1 and GM2.[42–45] However, such recorded sequences with strong ASs (resulting in significant damage accumulation) are rare in empirical databases. This may eventually affect the statistical robustness of developed fragility models.[46,47] To overcome this limitation while avoiding significant scaling of the considered earthquake records,[48,49] Aljawhari et al.[46] proposed a randomized approach (using Latin hypercube sampling) to assemble artificial GMS with as-recorded ground motions. Such GMSs represent multiple ground shaking that may occur in the form of typical MS-AS or even triggered events on nearby fault segments. A similar approach is adopted in this study,[50] consistently with the employed nonlinear analysis procedure (i.e., sequential cloud analysis) that relies on selecting ground motions covering a wide range of intensity levels without ensuring site-specific hazard consistency.

Specifically, this study uses the Pacific Earthquake Engineering Research (PEER) Center's NGA-West2 (*Enhancement of Next Generation Attenuation Relationships for Western US*) database[51,52] to assemble the GMS sets. Nearly 7000 unscaled (as-recorded) ground-motion records for active shallow tectonic regions are initially selected, removing those having very short significant durations (< 1 s). Both horizontal components are considered separately for each record with its unique record sequence number (RSN). The final seed ground-motion dataset contains 13,726 single-component records. These ground motions have moment magnitudes (M_w) ranging from 3.7 to 7.9, with source-to-site Joyner-Boore distances (R_{jb}) between 0.1 km and 600 km. The adopted record-selection method aims at selecting GM1–GM2 pairs from the seed dataset (as described above) to cover the largest range of possible $S_a(T_1)$ values for both GM1 and GM2, denoted $S_a(T_1)_{GM1}$ and $S_a(T_1)_{GM2}$, respectively. Light amplitude scaling is applied to this aim, with scaling factors SF_{GM1} and SF_{GM2} (to be determined) for GM1 and GM2, respectively. For each set of GM1, GM2, SF_{GM1}, and SF_{GM2}, a discrete two-dimensional distribution (i.e., histogram) with X bins along the $S_a(T_1)_{GM1}$ and $S_a(T_1)_{GM2}$ axes can be determined. X is selected to describe an adequate number of discrete $S_a(T_1)$ levels between zero and the maximum $S_a(T_1)$ value obtained from the seed database.

The simulated dual annealing approach[53,54] is finally utilized to minimize the following objective function:

$$obj = \ln\left[\frac{1}{X}\sum_{k=1}^{X}\left(x_k - \frac{\sum_{k=1}^{X}x_k}{X}\right)^2\right] \quad (1)$$

where, x_k is the number of ground motions in the k-th 2D bin. Minimizing Equation (1) results in a discrete distribution of $S_a(T_1)_{GM1}$ and $S_a(T_1)_{GM2}$, which is as close as possible to a uniform distribution. Therefore, the assembled GMS set can cover a uniform and wide range of $S_a(T_1)$ levels for both GM1 and GM2. The following constraints are also considered for the simulated annealing runs:

- The considered SF_{GM1} and SF_{GM2} values are within the range of 0.5–2.0 (i.e., light scaling) to avoid unrealistic ground-motion records due to significant scaling.[55]
- Each pair does not contain the same RSN of a record, that is, both horizontal components of a three-component ground motion are not used to assemble a sequence pair.[56]
- All pairs (RSN-GM1, RSN-GM2) are unique to avoid selecting the same pairs multiple times, and at least 70% of RSNs for GM1 and GM2 are different. This ensures the statistical independence of the data points used for fragility fitting. The higher the percentage selected for this constraint, the higher the computational time needed to minimize Equation (1). After some trials, 70% was chosen for this study to limit the computational time and obtain an adequate solution for most performed selections.

Figure 5 shows the scatter plots of the $S_a(T_1)_{GM1}$ and $S_a(T_1)_{GM2}$ values of the selected GMS sets. In this study, two sets of 800 GMS pairs are assembled for the 2- ($T_1 = 0.56$ s) and 4-story ($T_1 = 0.95$ s) archetype SMRFs, respectively. The number of GMSs in each set (i.e., 800) is chosen to provide a statistically significant number of ground-motion records of engineering relevance for the applications in this study and reduce the computational burden for the cloud-based NLTHAs. According to Figure 5, the portion of GMS with very larger $S_a(T_1)$ values (i.e., those larger than twice the corresponding $S_a(T_1)_{MCE}$ value) in both GM1 and GM2 is small. This is mainly due to the sparse nature of such strong ground motions and the applied constraints (as discussed above) for GMS selections. Finally, a 40-s free vibration between GM1
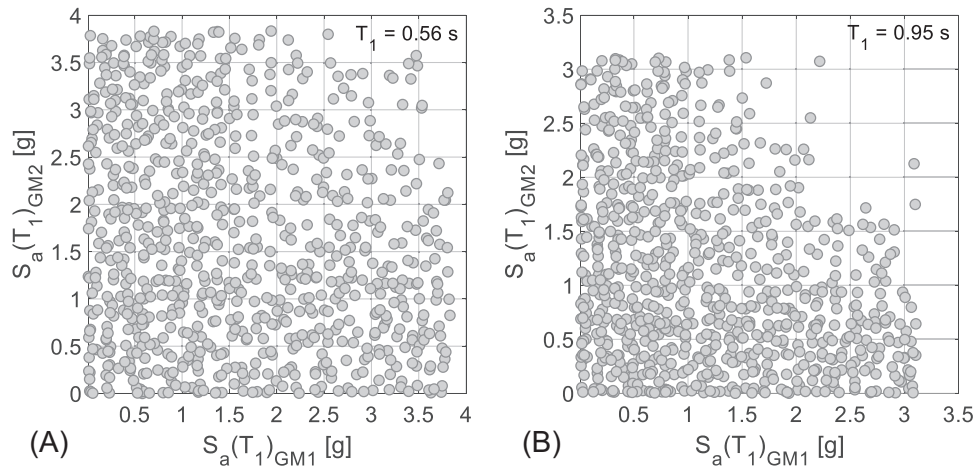
FIGURE 5   Scatter of the $S_a(T_1)$ values for the selected GM1 versus GM2: (A) 2-story frame ($T_1 = 0.56$ s); and (B) 4-story frame ($T_1 = 0.95$ s).

and GM2 of each selected pair is added to assemble the GMS for NLTHA. This time interval with zero acceleration is assumed sufficient to ensure that the 2- and 4-story frame models cease vibration (due to GM1) in dynamic analyses. It is worth noting that such a required time interval is strongly correlated with the fundamental period of the assessed structure.[57]

3 | NONLINEAR TIME HISTORY ANALYSIS

3.1 | SMRF collapse and ECBP connection failure criteria

As mentioned in Section 2.1, two sets of 2- and 4-story SMRF models (three in each set) are developed with proposed ECBP connections designed for three distinct strength levels (i.e., $R = 8$; $\Omega = 3$; and $1.1R_yM_p$). In addition, cloud-based NLTHAs for each frame are performed using the selected suite of 800 GMSs (Section 2.3). These analyses provide quantitative estimates of BCF and global collapse probabilities under earthquake-induced ground shaking.

As per FEMA P695,[58] global collapse is conventionally considered the sole criterion for unacceptable response (or failure criterion) in the context of the frame seismic performance. This is typically characterized as extreme lateral deformations in a sidesway mode due to hinges at the beam/column ends. In this study, it is assumed to occur when the interstory drift ratio (IDR) in any story exceeds 10%. This conventional collapse indicator provides a drift threshold from which recovery is improbable,[59,60] and it also avoids computationally intensive simulations of frame "down to the earth" (e.g., as done for incremental dynamic analysis[61]).

In addition, the current study considers the BCF of the ECBP connections. The post-failure response of ECBP connection and its effects on the frame seismic performance (i.e., global collapse) are also considered. According to Hassan et al.,[13] two possible failure modes of the proposed ECBP connection detail (with ductile anchor rods) were identified, and their failure prediction models were developed. Each of them is briefly discussed below:

- Anchor necking-induced failure: necking of the UT anchor section (which occurs on a tensile excursion) causes strength loss and rapid localization of strains within the necked region, ultimately leading to fracture. The damage index to predict the necking occurrence (D_{neck}) is expressed as follows:

$$D_{neck} = \frac{\varepsilon_{max}}{\varepsilon_{neck}} \tag{2}$$

where, ε_{max} is the maximum tensile strain achieved until any point in the time history of the UT section, and ε_{neck} is the strain value at which necking would initiate, such that D_{neck} exceeding one indicates necking. As per ASTM 1554,[27] ε_{neck} is computed as 0.11 for Gr.105 steel (used for anchor rods in this study). This ε_{neck}-value and the associated ultimate tensile strength (= 947 MPa, obtained from the uniaxial tensile tests of the proposed anchor rods in Hassan et al.[13]) are

employed to represent the cap of the rod material model (as discussed in Section 2.2). It is worth noting that the use of Equation (2) disregards history effects to predict the necking occurrence of cyclically and axially loaded anchor rods. However, due to the stabilization of hysteresis loops before reaching $\varepsilon_{\text{neck}}$, the tensile strain interpreted in a monotonic manner (e.g., ε_{max} in Equation (2)) is a relatively accurate predictor of the instantaneous stress and tangent modulus, which jointly control the necking instability.[13]

- Anchor ULCF fracture: in the cases that single tensile cycles (during seismic events) are not large enough to trigger necking, ULCF fracture may still occur due to cyclic plastic strain that homogenously accumulates over the total length of the UT section. Kanvinde[62] has comprehensively reviewed several available continuum damage mechanics-based models to predict ULCF fracture. In this study, the stress-weighted damage fracture model (SWDFM)[63] is adopted to assess ULCF damage. For the uniaxial cyclic case with an axisymmetric state of stress (i.e., the expected loading condition of the anchor UT region), the damage index for ULCF (D_{ULCF}) may be expressed as follows:

$$D_{\text{ULCF}} = \int_0^{\varepsilon_p} C \cdot [2 \cdot \exp(1.3T) - \exp(-1.3T)] \cdot d\varepsilon_p \tag{3}$$

where, T is the triaxiality that alternates between 1/3 for tension and −1/3 for compression, $d\varepsilon_p$ is the incremental plastic strain, and C is a calibrated material parameter. Smith et al.[63] reported C-values for various structural steel materials, and $C = 0.31$ (the largest value reported) is selected to conservatively estimate the ULCF damage. Similar to D_{neck}, D_{ULCF} exceeding one predicts ULCF failure. It is worth noting that Equation (3) is a simplified expression of the original SWDFM model. A multiplier ($= 1$) in the integral of the original form (i.e., an exponential function of the difference between the absolute value of the Lode parameter and one; and the Lode parameter equals ±1 for axisymmetric tension and compression cases herein) is removed in Equation (3).

All terms in Equations (2) and (3) may be known (e.g., $\varepsilon_{\text{neck}}$, and C) or readily determined (e.g., ε_{max}, T, and $d\varepsilon_p$) from the anchor rod load-deformation (or stress–strain) histories monitored from LEB base connection models. It is assumed that the attainment of either failure mode (i.e., D_{neck} or D_{ULCF} reaches one) indicates the ECBP connection failure (i.e., BCF). In addition, the bending failure of the base plate is not anticipated to be a possible damage mode. This is because the proposed ECBP detail drives the cyclic inelastic deformations into the designated yielding anchor rods (using UT sections), and the base plate is designed much stronger than the anchor rods to remain elastic (see Section 2.1).

3.2 | NLTHA results and discussions

In this study, the two damage indices (i.e., D_{neck} and D_{ULCF}, to infer damage in the anchor rods), along with IDR (to check frame sidesway collapse), are considered as engineering demand parameters (EDPs) for seismic performance assessment of the considered SMRFs. Various analysis outputs in the form of time histories are monitored during the NLTHAs of each SMRF subjected to the selected GMS suite; these include (1) the IDR and its maximum value (MIDR) of each run; (2) the axial force, moment, and rotation at each ECBP connection level to record seismic demands of ECBP connections; and (3) the axial force and deformation (elongation) of UT segment in each anchor rod to compute the D_{neck} and D_{ULCF} damage indices. The D_{neck} and D_{ULCF} calculation in the postprocessing is terminated if sidesway collapse of the frame occurs (i.e., MIDR reaches 0.1) in the same run. Calculating damage indices in this manner allows one to determine whether the BCF leads to the frame collapse.

Figure 6A–C shows the computed D_{neck} versus D_{ULCF} values (i.e., the maximum values obtained among the four ECBP connections of each frame and each run) of all the three considered 4-story SMRFs (with the ECBP connections designed for strengths of $R = 8$; $\Omega = 3$; and $1.1R_y M_p$) subjected to GM1 only. The results for each frame are plotted as cloud points in each panel, and the red points highlight the collapse cases. The red dashed lines in Figure 6A represent damage indices equal to one; therefore, the points outside these thresholds indicate ECBP connection failure. An identity line is also displayed (i.e., the black dotted line) to compare two damage indices in each NLTHA run. Referring to Figure 6, the following observations may be made:

- Figure 6A illustrates large damage indices of the $R = 8$ strength case because this case corresponds to the weak-base design, and the inelastic deformation of the anchor rod under seismic excitation is expected. On the other hand, when
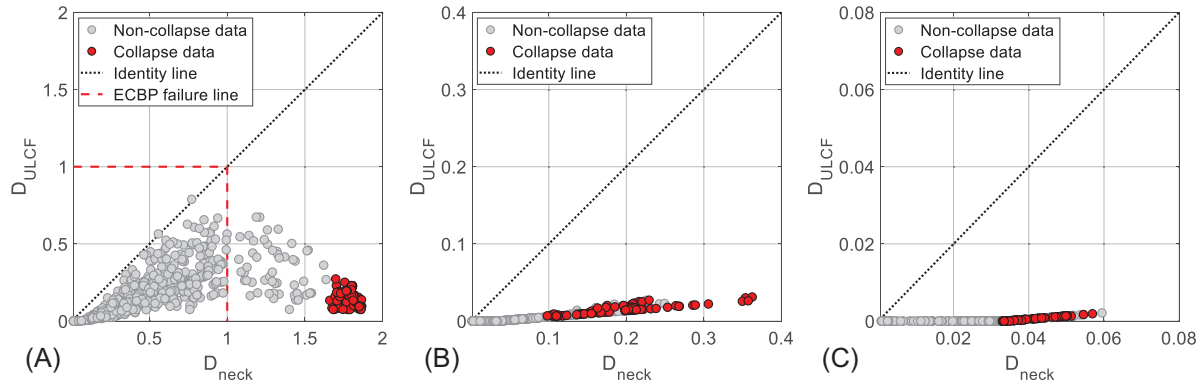
FIGURE 6 Scatter of D_{neck} versus D_{ULCF} for 4-story frames obtained from cloud-based NLTHAs of GM1, with three considered strength levels of ECBP connections: (A) $R = 8$; (B) $\Omega = 3$; and (C) $1.1R_yM_p$.

the ECBP connection is designed for the $1.1R_yM_p$ strength, the inelastic deformation demand of the anchor rods is limited, resulting in negligible D_{neck} and D_{ULCF} values (see Figure 6C). This is not surprising because the ECBP connections are capacity-designed, and their seismic response is highly elastic. According to Figure 6B, both D_{neck} and D_{ULCF} values for the $\Omega = 3$ strength cases are larger than those of capacity-designed cases, but they are still far less than one. This is mainly because the $\Omega = 3$ strength of the bottom column in the considered 4-story SMRF (for base connection design) is fairly close to $1.1R_yM_p$, (see Table 1), such that the hardening ECBP connections end up pushing significant rotation into the connected column.

- The necking-induced anchor rod failure (i.e., points with $D_{neck} > 1$) can be observed for the $R = 8$ strength case in Figure 6A, while the anchor rods are unlikely to exhibit ULCF fracture subjected to a single ground motion. Even under significantly strong ground motions having $S_a(T_1)_{GM1}$ values larger than twice the corresponding 2/50-hazard value, the maximum D_{ULCF} value found for $R = 8$ strength case is lower than 0.8.

- For the weak-base designed case (i.e., $R = 8$ strength case), necking failure of anchor rods may be considered the dominant failure mode of the proposed ductile ECBP connection detail. This can be confirmed in Figure 6A, because (1) only necking failure is observed for the 800 NLTHA runs; and (2) most of the points in Figure 6A (with only two exceptions) are located in the lower region as per the identity line, indicating that the D_{neck} values of these points are larger than their corresponding D_{ULCF} values.

- For the weak-base designed case (see Figure 6A), all the points of frame collapse (i.e., the red points) show D_{neck} values larger than 1.6. This may be interpreted as the base connection failing before the frame sideway collapse. A closer investigation reveals that this archetype SMRF may not collapse even when all the ductile base connections fail due to necking in the anchors (i.e., each of the ECBP connections has $1 < D_{neck} < 1.6$). This observation is attributed to the shear integrity that the ECBP connections may still maintain (e.g., through shear key), even though they entirely lose the rotational capacity. As mentioned in Section 2.2, the shear force in the base during NLTHAs may be transferred through the lateral supports in the LEB model (see Figure 4).

- The frame designed with strong bases (i.e., $1.1R_yM_p$ strength case) always fails due to the global instability, while the ECBP connections remain intact (see the red points in Figure 6C). The same finding is held for this specific 4-story frame with ECBP connections designed per $\Omega = 3$ strength.

The observations from all three strength cases of the 2-story archetype frames (subjected to the GM1s only) are similar to those of the 4-story SMRFs reported above. According to Table 1, the overstrength moments (i.e., $\Omega = 3$ case) determined at the bases of the considered 2-story SMRF is slightly larger than the capacity-based moments (i.e., $1.1R_yM_p$ case). This results in even lower (and negligible) D_{neck} and D_{ULCF} values for the $\Omega = 3$ strength case. For the sake of brevity, D_{neck} versus D_{ULCF} results are not shown here.

Figure 7A,B illustrates the computed D_{neck} versus D_{ULCF} values of 2- and 4-story archetype SMRFs subjected to the GMSs (i.e., GM1+GM2), respectively. Only the results of frames with the ECBP connections designed for $R = 8$ strength (i.e., weak-base design) are provided in Figure 7. It should be noted that the collapse and BCF points due to GM1 have been removed from Figure 7. Referring to Figure 7, some findings are discussed as follows:
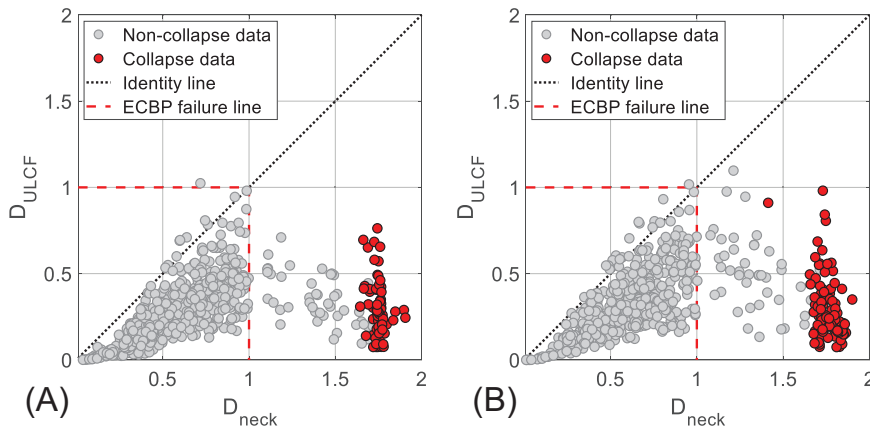
FIGURE 7 Scatter of D_{neck} versus D_{ULCF} for (A) 2-story frame; and (B) 4-story frame obtained from cloud-based NLTHAs of GMS, with $R = 8$ strength levels of ECBP connections.

- A comparison between Figures 6A and 7B (for the same 4-story frame with base connections designed for $R = 8$ strength) indicates that the increase of D_{ULCF} values is evident if a second ground motion is assumed to shake the SMRF following a first one. This is because D_{ULCF} is calculated in a cumulative sense (as per Equation (3)), and it would increase if GM2 is strong enough to cause inelastic deformation in the anchor rods of the base connections.
- Due to the plastic strain accumulation of D_{ULCF} during GM2, some points in Figure 7A,B display larger D_{ULCF} values than their D_{neck} counterparts; these can be observed as the points exceed the identity line. Three points (one in Figure 7A and two in Figure 7B) have D_{ULCF} values exceeding the unit, and two cases of ECBP failure (one in each panel) are attributed to the ULCF fracture of ductile anchor rods. A closer examination indicates that (1) the relatively low flexural strength of the ECBP connection; and (2) the strong ground motions (both GM1 and GM2 with spectral accelerations larger than the corresponding MCE value) featuring relatively long durations may result in the observed ULCF fracture. However, this observation is still rare.
- Anchor rod necking is still the dominant failure mode of the proposed ductile ECBP connections, even though two ground motions in series are applied for the archetype SMRFs.
- Similar to the GM1-based results in Figure 6A, the D_{neck} values (for the weak-design cases) corresponding to the frame collapse are significantly larger than one. Due to the maintenance of shear integrity in base connections, global collapse may not occur immediately after the BCF.

The GMS-based results of two damage indices for $\Omega = 3$ and $1.1R_yM_p$ strength cases are not displayed in Figure 7 because the ECBP connections of these two cases are designed with very large loads, resulting in almost elastic responses of base connections and anchors during each GMS. This indicates that only negligible D_{neck} and D_{ULCF} values can be observed, and the resulting plots are quantitatively similar to Figure 6B,C (i.e., the GM1-based plots).

To further assess the base rotation capacity of the proposed ductile ECBP connections, the base rotation achieved when the corresponding ECBP connection fails (i.e., $D_{neck} = 1$ or $D_{ULCF} = 1$) is checked in each NLTHA run. It is worth noting that the BCF data collected from both GM1 and GM2 are pooled together for each weak-base designed frame to determine the rotational capacity. The average base rotations achieved at $D_{neck} = 1$ for the 2- and 4-story frames are 0.068 and 0.064 rad, respectively. Variations of these two rotations, measured by the coefficient of variation (CoV, i.e., the ratio of standard deviation to the mean), are very small (i.e., CoV is about 2%). Therefore, 0.06 rad may be conservatively considered as the rotation capacity of the proposed ECBP connections if (1) the ratio of the stretch length of the anchor UT region to base plate length is 1/2 (see Section 2.1); and (2) the necking induced failure is the desirable failure mode of the ductile base connections. In addition, the associated base rotations at $D_{ULCF} = 1$ for the 2- and 4-story frames (one case in each frame) are 0.047 and 0.058 rad, respectively. They are lower than the assumed capacity (∼0.06 rad) that can be achieved due to necking-induced failure. It implies that the ULCF fracture of anchors may be the unfavorable failure mode of the proposed ECBP connection detail, leading to the BCF with less anticipated and unstable ductility. However, this failure mode is improbable (as discussed above).

Moreover, the number of collapse cases for each frame subjected to the same GMS suite and the story that first reaches the 10%-IDR threshold in each run is checked from the NLTHA results. For both 2- and 4-story frame sets, the total collapse numbers of $R = 8$ strength cases (i.e., weak-base cases) are much larger than those of $\Omega = 3$ and $1.1R_yM_p$ strength cases (i.e., strong-base cases), while the latter two design cases have comparable collapse numbers. It is also found that the

proportions of first-story collapses of 2- and 4-story frames with weak-base designs are considerably high (i.e., 100% and 99.6% for 2- and 4-story frames, respectively). It indicates that the frames with weak bases (exhibiting high rotational flexibility) may alter the frame response by shifting the point of inflection to the lower region of the first-story column, leading to a soft-story collapse mechanism.[20] Regarding the frames with base connections designed for overstrength or capacity-based loads, first-story collapse is not always the case because the collapse mechanisms of these frames usually involve the full participation of structure.[20]

4 | SEISMIC FRAGILITY ASSESSMENT

4.1 | Formulation of fragility models

In this section, a procedure for calculating the probabilities of BCF and frame collapse (as defined in Section 3.1) due to one ground motion (i.e., GM1) and two ground motions (i.e., GM1 + GM2) in a sequence (i.e., GMS), as well as the associated fragility curves (for GM1 only) and fragility surfaces (for GMS) are presented.

Let $P^{\text{GMS}}[\text{BCF}|S_a(T_1)_{\text{GM1}}, S_a(T_1)_{\text{GM2}}]$ be the BCF probability given a GMS, and GMS is assembled by GM1 with $S_a(T_1)_{\text{GM1}}$ and GM2 with $S_a(T_1)_{\text{GM2}}$. Similar to the formulation of limit-state exceedance probability due to MS-AS sequence,[64,65] the probability of BCF due to GMS can be further broken down as follows: the base connection fails due to GM1 with the probability $P^{\text{GM1}}[\text{BCF}|S_a(T_1)_{\text{GM1}}]$, or it fails with probability $P^{\text{GM2}}[\text{BCF}|S_a(T_1)_{\text{GM1}}, S_a(T_1)_{\text{GM2}}]$ during GM2, given that the base connection does not fail due to GM1. By using the total probability theorem, $P^{\text{GMS}}[\text{BCF}|S_a(T_1)_{\text{GM1}}, S_a(T_1)_{\text{GM2}}]$ can be expressed as:

$$
\begin{aligned}
P^{\text{GMS}}\left[\text{BCF}|S_a(T_1)_{\text{GM1}}, S_a(T_1)_{\text{GM2}}\right] &= P^{\text{GM1}}\left[\text{BCF}|S_a(T_1)_{\text{GM1}}\right] \\
&+ \left(1 - P^{\text{GM1}}\left[\text{BCF}|S_a(T_1)_{\text{GM1}}\right]\right) \cdot P^{\text{GM2}}\left[\text{BCF}|S_a(T_1)_{\text{GM1}}, S_a(T_1)_{\text{GM2}}\right]
\end{aligned}
\tag{4}
$$

The term $P^{\text{GM1}}[\text{BCF}|S_a(T_1)_{\text{GM1}}]$ in Equation (4) represents the BCF fragility (curve) for GM1 only with respect to $S_a(T_1)_{\text{GM1}}$, and the term $(1 - P^{\text{GM1}}[\text{BCF}|S_a(T_1)_{\text{GM1}}])$ is its complementary fragility, indicating the probability of no BCF due to GM1 given specific spectral intensity values. These two terms can be determined by applying the standard cloud analysis only to the portion of GM1 record suite. According to Section 3.1, two EDPs (i.e., D_{neck} and D_{ULCF}) are needed to determine the violation of the BCF limit state. As a result, $P^{\text{GM1}}[\text{BCF}|S_a(T_1)_{\text{GM1}}]$ can be expressed as follows, depending on both necking and ULCF failure modes:

$$
\begin{aligned}
P^{\text{GM1}}\left[\text{BCF}|S_a(T_1)_{\text{GM1}}\right] &= P^{\text{GM1}}\left[D_{\text{neck}} > 1|S_a(T_1)_{\text{GM1}}\right] + P^{\text{GM1}}\left[D_{\text{ULCF}} > 1|S_a(T_1)_{\text{GM1}}\right] \\
&- P^{\text{GM1}}\left[D_{\text{neck}} > 1 \cap D_{\text{ULCF}} > 1|S_a(T_1)_{\text{GM1}}\right]
\end{aligned}
\tag{5}
$$

where, $P^{\text{GM1}}[D_{\text{neck}} > 1|S_a(T_1)_{\text{GM1}}]$ and $P^{\text{GM1}}[D_{\text{ULCF}} > 1|S_a(T_1)_{\text{GM1}}]$ are the fragility functions of necking and ULCF failure of ECBP connections, derived from cloud data of GM1-record cases through NLTHAs. In this study, the well-known power-law model[66] is adopted in the cloud analysis, which can be expressed as follows:

$$
D_* = a_0 \cdot \left[S_a(T_1)_{\text{GM1}}\right]^{a_1}
\tag{6}
$$

where, D_* represents either D_{neck} or D_{ULCF}, and the asterisk subscript denotes the specific failure mode of the base connection. Equation (6) can be re-written as a linear expression of the natural logarithmic forms of D_* and $S_a(T_1)_{\text{GM1}}$:

$$
\ln(D_*) = \ln(a_0) + a_1 \cdot \ln\left[S_a(T_1)_{\text{GM1}}\right] + e
\tag{7}
$$

In both Equations (6) and (7), a_0 and a_1 are the regression parameters, and e in Equation (7) is a zero-mean random variable representing the variability of $\ln(D_*)$ given $S_a(T_1)_{\text{GM1}}$. This logarithmic transformation assumes that D_* (i.e., EDP) is conditionally lognormally distributed (conditional on the values of IM, in this case, $S_a(T_1)_{\text{GM1}}$). Following this common assumption, the necking/ULCF failure probability of ECBP connection considering only GM1-based results,

that is, $P^{\text{GM1}}[D_* > 1|S_a(T_1)_{\text{GM1}}]$, can be estimated through the IM-basis closed-form solution of a lognormal function[67]:

$$P^{\text{GM1}} \left[D_* > 1 \left| S_a(T_1)_{\text{GM1}} \right. \right] = \Phi \left(\frac{\ln \left[S_a(T_1)_{\text{GM1}} \right] - \ln \left[(1/a_0)^{1/a_1} \right]}{\sigma_{\ln(D_*)|S_a(T_1)_{\text{GM1}}} / a_1} \right) \tag{8}$$

where, $(1/a_0)^{1/a_1}$ is the $S_a(T_1)_{\text{GM1}}$ value corresponding to the seismic capacity of D_* (= 1) with a 50% probability of exceedance (i.e., the median of the fragility function), and $\sigma_{\ln(D_*)|S_a(T_1)_{\text{GM1}}}$ is the standard deviation of the linear regression-based probabilistic model (i.e., Equation (7)), which is assumed to be constant with respect to all $S_a(T_1)_{\text{GM1}}$ levels in the cloud analysis:

$$\sigma_{\ln(D_*)|S_a(T_1)_{\text{GM1}}} = \sqrt{\frac{\sum_{i=1}^{N_{rec}} \left[\ln(D_*)_i - \left(\ln(a_0) + a_1 \cdot \ln \left[S_a(T_1)_{\text{GM1}} \right]_i \right) \right]^2}{N_{rec} - 2}} \tag{9}$$

where, N_{rec} is the total number of GM1 records through NLTHAs, $(D_*)_i$ and $[S_a(T_1)_{\text{GM1}}]_i$ are the damage index (i.e., D_{neck} or D_{ULCF}) and $S_a(T_1)_{\text{GM1}}$ values corresponding to the i-th GM1 record. Then, the terms $P^{\text{GM1}}[D_{\text{neck}} > 1|S_a(T_1)_{\text{GM1}}]$ and $P^{\text{GM1}}[D_{\text{ULCF}} > 1|S_a(T_1)_{\text{GM1}}]$ in Equation (5) can be determined through Equations (6)–(9). It should be noted that the estimated a_0 and a_1 values for D_{neck}–$S_a(T_1)_{\text{GM1}}$ and D_{ULCF}–$S_a(T_1)_{\text{GM1}}$ relationships are based on their own cloud-based NLTHA data and, therefore, are not the same. Finally, the only practical difficulty may lie in computing the last term in Equation (5), that is, $P^{\text{GM1}}[D_{\text{neck}} > 1 \cap D_{\text{ULCF}} > 1|S_a(T_1)_{\text{GM1}}]$, which is the probability of the intersection of necking and ULCF failures. Given the fact that the capacities of these two failure modes are independent, the intersection may be estimated through the product of the two individual probabilities[67]:

$$P^{\text{GM1}} \left[D_{\text{neck}} > 1 \cap D_{\text{ULCF}} > 1 \left| S_a(T_1)_{\text{GM1}} \right. \right] = P^{\text{GM1}} \left[D_{\text{neck}} > 1 \left| S_a(T_1)_{\text{GM1}} \right. \right] \cdot P^{\text{GM1}} \left[D_{\text{ULCF}} > 1 \left| S_a(T_1)_{\text{GM1}} \right. \right] \tag{10}$$

Equations (5)–(10) formulate the fragility model (curve) of BCF for GM1 only, that is, $P^{\text{GM1}}[\text{BCF}|S_a(T_1)_{\text{GM1}}]$ in Equation (4).

Similar to the formulation of Equation (5), the last term $P^{\text{GM2}}[\text{BCF}|S_a(T_1)_{\text{GM1}}, S_a(T_1)_{\text{GM2}}]$ in Equation (4) (i.e., the fragility function of BCF due to GM2, given no base failure occurring due to GM1) can be written as follows:

$$\begin{aligned} P^{\text{GM2}} \left[\text{BCF} \left| S_a(T_1)_{\text{GM1}}, S_a(T_1)_{\text{GM2}} \right. \right] &= P^{\text{GM2}} \left[D_{\text{neck}} > 1 \left| S_a(T_1)_{\text{GM1}}, S_a(T_1)_{\text{GM2}} \right. \right] \\ &+ P^{\text{GM2}} \left[D_{\text{ULCF}} > 1 \left| S_a(T_1)_{\text{GM1}}, S_a(T_1)_{\text{GM2}} \right. \right] \\ &- P^{\text{GM2}} \left[D_{\text{neck}} > 1 \cap D_{\text{ULCF}} > 1 \left| S_a(T_1)_{\text{GM1}}, S_a(T_1)_{\text{GM2}} \right. \right] \end{aligned} \tag{11}$$

where, $P^{\text{GM2}}[D_{\text{neck}} > 1|S_a(T_1)_{\text{GM1}}, S_a(T_1)_{\text{GM2}}]$ and $P^{\text{GM2}}[D_{\text{ULCF}} > 1|S_a(T_1)_{\text{GM1}}, S_a(T_1)_{\text{GM2}}]$ are the fragility models of necking and ULCF failure due to GM2, respectively. It is noted that Equation (11) is valid only if the base connections do not fail during GM1, which implies that (1) the considered IM of GM1 (i.e., $S_a(T_1)_{\text{GM1}}$) would also affect the derivation of Equation (11); and (2) only the portion of cloud data (obtained from NLTHAs for the GMS suite) which does not cause BCF during GM1 is applied to determine these terms. A bivariate power-law model[65] is used to determine them, and it is expressed as follows:

$$D_* = b_0 \cdot \left[S_a(T_1)_{\text{GM1}} \right]^{b_1} \cdot \left[S_a(T_1)_{\text{GM2}} \right]^{b_2} \tag{12}$$

and it can be re-written in a natural logarithmic form as follows:

$$\ln(D_*) = \ln(b_0) + b_1 \cdot \ln \left[S_a(T_1)_{\text{GM1}} \right] + b_2 \cdot \ln \left[S_a(T_1)_{\text{GM2}} \right] + e \tag{13}$$

where, D_* has the same meaning of it in Equation (6), e is a zero-mean random variable representing the variability of $\ln(D_*)$ given $S_a(T_1)_{\text{GM1}}$ and $S_a(T_1)_{\text{GM2}}$, and b_0, b_1, b_2 are the parameters of the linear logarithmic regression. According to Equations (12) and (13), the necking/ULCF fragility function due to GM2, given non-BCF in GM1 condition, that is,

$P^{\text{GM2}}[D_* > 1 | S_a(T_1)_{\text{GM1}}, S_a(T_1)_{\text{GM2}}]$, can be expressed as a lognormal function:

$$P^{\text{GM2}}\left[D_* > 1 \,\middle|\, S_a(T_1)_{\text{GM1}}, S_a(T_1)_{\text{GM2}}\right] = \Phi\left(\frac{\ln\left[S_a(T_1)_{\text{GM2}}\right] - \ln\left[\left(1/\left(b_0 \cdot \left[S_a(T_1)_{\text{GM1}}\right]^{b_1}\right)\right)^{1/b_2}\right]}{\sigma_{\ln(D_*)|S_a(T_1)_{\text{GM1}},S_a(T_1)_{\text{GM2}}}/b_2}\right) \quad (14)$$

where, $(1/(b_0 \cdot [S_a(T_1)_{\text{GM1}}]^{b_1}))^{1/b_2}$ is the $S_a(T_1)_{\text{GM2}}$ value corresponding to the seismic capacity of D_* (= 1) and conditioned on a specific $S_a(T_1)_{\text{GM1}}$ value, with 50% exceeding probability; and $\sigma_{\ln(D_*)|S_a(T_1)_{\text{GM1}},S_a(T_1)_{\text{GM2}}}$ is the standard deviation of the linear regression model of Equation (13). The latter is assumed to be constant to the range of $S_a(T_1)_{\text{GM2}}$ values, given each specific $S_a(T_1)_{\text{GM1}}$ level in the fragility model:

$$\sigma_{\ln(D_*)|S_a(T_1)_{\text{GM1}},S_a(T_1)_{\text{GM2}}} = \sqrt{\frac{\sum_{i=1}^{N_{rec}}\left[\ln(D_*)_i - \left(\ln(b_0) + b_1 \cdot \ln\left[S_a(T_1)_{\text{GM1}}\right]_i + b_2 \cdot \ln\left[S_a(T_1)_{\text{GM2}}\right]_i\right)\right]^2}{N_{rec} - 2}} \quad (15)$$

where, N_{rec} represents the total number of records selected for computing $P^{\text{GM2}}[D_* > 1 | S_a(T_1)_{\text{GM1}}, S_a(T_1)_{\text{GM2}}]$; $(D_*)_i$, $[S_a(T_1)_{\text{GM1}}]_i$ and $[S_a(T_1)_{\text{GM2}}]_i$ are the damage index, $S_a(T_1)_{\text{GM1}}$ and $S_a(T_1)_{\text{GM2}}$ values associated with the i-th ground motion sequence. The terms $P^{\text{GM2}}[D_{\text{neck}} > 1 | S_a(T_1)_{\text{GM1}}, S_a(T_1)_{\text{GM2}}]$ and $P^{\text{GM2}}[D_{\text{ULCF}} > 1 | S_a(T_1)_{\text{GM1}}, S_a(T_1)_{\text{GM2}}]$ in Equation (11) now can be computed following Equations (12)–(15). Again, the fitted parameter sets (i.e., b_0, b_1, and b_2) are different for the bivariate models of D_{neck} and D_{ULCF}.

Special attention should be paid to selecting the cloud data for estimating $P^{\text{GM2}}[D_{\text{neck}} > 1 | S_a(T_1)_{\text{GM1}}, S_a(T_1)_{\text{GM2}}]$ because D_{neck} is not a cumulative EDP but a peak-value-based one. Based on Equation (2), D_{neck} value obtained after GM2 may keep identical to the value from GM1 in the same GMS if the maximum strain ($\varepsilon_{\max}$) achieved in GM2 is not larger than that of GM1. These are frequently observed when GM1 and GM2 of a sequence have $S_a(T_1)_{\text{GM2}} << S_a(T_1)_{\text{GM1}}$, as discussed by Aljawhari et al.[46] when investigating MIDR demands for case-study buildings subjected to GMSs. In particular, Aljawhari et al.[46] demonstrated that (1) a bilinear fitting of the EDPs versus IMs cloud data could effectively help address those issues; and (2) the model fitting corresponding to $S_a(T_1)_{\text{GM2}} << S_a(T_1)_{\text{GM1}}$ (generally corresponding to the first branch of the bilinear model) has a negligible contribution to overall fragility models for the case-study buildings. Hence, consistently with the findings from Aljawhari et al.,[46] only cloud points corresponding to $S_a(T_1)_{\text{GM2}} > S_a(T_1)_{\text{GM1}}$ are arbitrarily selected in this study from the original dataset for GM2 (which has been discussed when introducing Equation (11)) for predicting the necking failure probability due to GM2. This assumption is not expected to significantly affect the analysis results or to produce any significant bias in the resulting fragility models. However, it may slightly overestimate the necking failure fragility in the region having $S_a(T_1)_{\text{GM2}} < S_a(T_1)_{\text{GM1}}$. An example of this derivation is given in Section 4.3. On the other hand, the full cloud-point set for GM2 (with non-BCF due to GM1) is applied to estimate $P^{\text{GM2}}[D_{\text{ULCF}} > 1 | S_a(T_1)_{\text{GM1}}, S_a(T_1)_{\text{GM2}}]$, since D_{ULCF} is a cumulative EDP.

Finally, the last term in Equation (11), that is, $P^{\text{GM2}}[D_{\text{neck}} > 1 \cap D_{\text{ULCF}} > 1 | S_a(T_1)_{\text{GM1}}, S_a(T_1)_{\text{GM2}}]$, can be computed following the same assumption for Equation (10):

$$P^{\text{GM2}}\left[D_{\text{neck}} > 1 \cap D_{\text{ULCF}} > 1 \,\middle|\, S_a(T_1)_{\text{GM1}}, S_a(T_1)_{\text{GM2}}\right] = P^{\text{GM2}}\left[D_{\text{neck}} > 1 \,\middle|\, S_a(T_1)_{\text{GM1}}, S_a(T_1)_{\text{GM2}}\right]$$
$$\cdot P^{\text{GM2}}\left[D_{\text{ULCF}} > 1 \,\middle|\, S_a(T_1)_{\text{GM1}}, S_a(T_1)_{\text{GM2}}\right] \quad (16)$$

Equations (11)–(16) provide the method to compute $P^{\text{GM2}}[\text{BCF}|S_a(T_1)_{\text{GM1}}, S_a(T_1)_{\text{GM2}}]$ in Equation (4). In summary, the fragility surface represented by $P^{\text{GMS}}[\text{BCF}|S_a(T_1)_{\text{GM1}}, S_a(T_1)_{\text{GM2}}]$, that is, BCF failure probability due to both GM1 and GM2 in a sequence (so-called GMS in this study), can be derived using Equations (4)–(16) above.

Regarding the collapse (denoted Col in the following terms) fragility model for GM1, that is, $P^{\text{GM1}}[\text{Col}|S_a(T_1)_{\text{GM1}}]$, a logistic regression (a.k.a., logit) model as a function of $S_a(T_1)_{\text{GM1}}$ is used to formulate it[56,64]:

$$P^{\text{GM1}}\left[\text{Col}\,\middle|\,S_a(T_1)_{\text{GM1}}\right] = \frac{1}{1 + \exp\left[-\left(\alpha_0 + \alpha_1 \cdot S_a(T_1)_{\text{GM1}}\right)\right]} \quad (17)$$
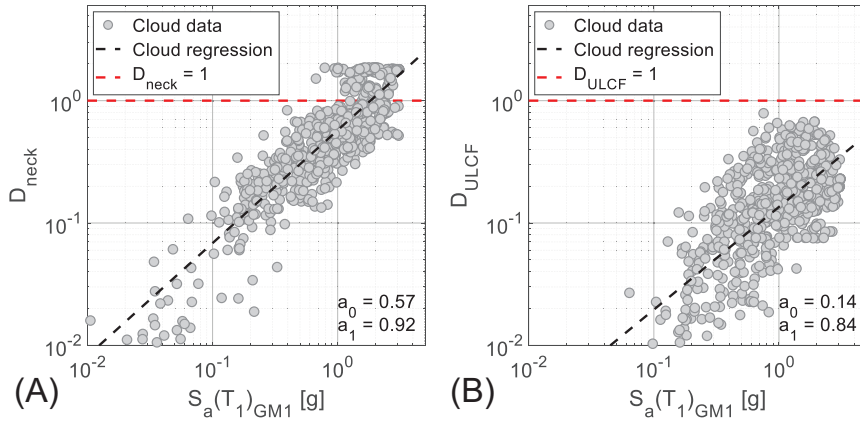
FIGURE 8 Cloud regression for 4-story frame with $R = 8$ strength level of ECBP connections, considering cloud data of GM1 set only: (A) D_{neck} versus $S_a(T_1)_{GM1}$; and (B) D_{ULCF} versus $S_a(T_1)_{GM1}$.

where α_0 and α_1 are the logistic regression parameters. It is to note that the logit model described by Equation (17) is applied to all GM1 records (i.e., a total of 800 in this study), and is particularly useful if the regression dependent variable is binary (i.e., only have two values 1 and 0, corresponding to the cases of collapse and non-collapse herein).

Using the same concept for deriving Equation (4), the frame collapse probability given a GMS, that is, $P^{GMS}[\text{Col}|S_a(T_1)_{GM1}, S_a(T_1)_{GM2}]$, may be written as follows. This is, again, an application of the total probability theorem:

$$
\begin{aligned}
P^{GMS}\left[\text{Col}\,|S_a(T_1)_{GM1}, S_a(T_1)_{GM2}\right] &= P^{GM1}\left[\text{Col}\,|S_a(T_1)_{GM1}\right] \\
&+ \left(1 - P^{GM1}\left[\text{Col}\,|S_a(T_1)_{GM1}\right]\right) \cdot P^{GM2}\left[\text{Col}\,|S_a(T_1)_{GM1}, S_a(T_1)_{GM2}\right]
\end{aligned}
\tag{18}
$$

where, the term $P^{GM1}[\text{Col}|S_a(T_1)_{GM1}]$ is determined through Equation (17), and the term $P^{GM2}[\text{Col}|S_a(T_1)_{GM1}, S_a(T_1)_{GM2}]$ (i.e., the collapse probability due to GM2, given no collapse during GM1) may be estimated using a multiple logistic regression model,[68] which is a function of both $S_a(T_1)_{GM1}$ and $S_a(T_1)_{GM2}$:

$$
P^{GM2}\left[\text{Col}\,|S_a(T_1)_{GM1}, S_a(T_1)_{GM2}\right] = \frac{1}{1 + \exp\left[-\left(\beta_0 + \beta_1 \cdot S_a(T_1)_{GM1} + \beta_2 \cdot S_a(T_1)_{GM2}\right)\right]}
\tag{19}
$$

where, β_0, β_1, and β_2 are fitting parameters of the logistic regression. To summarize, the collapse fragility surface of GMS (i.e., a sequence of GM1 followed by GM2) can be derived through Equations (17)–(19).

4.2 | Fragility assessment of SMRFs with ductile ECBPs subject to single ground motions

For illustrative purposes, Figure 8 shows the cloud regressions (i.e., Equations (6)–(7)) for the 4-story archetype SMRF (with ECBP connections designed for $R = 8$ strength level) using the set of GM1 records (Section 2.3). For each scatter plot, the regression lines (black dashed lines) are fitted to the cloud data. The red dashed lines of $D_{neck} = 1$ and $D_{ULCF} = 1$, showing the onset of necking failure and ULCF failure, are also given in the corresponding panels. Figure 9A depicts the fragility curves (in blue) for necking and ULCF failures, their intersection, and the associated BCF (base connection failure) derived from Figure 8. It can be observed that the necking fragility is significantly higher than the ULCF fragility (which has negligible fragility values) for the weak-base designed case (e.g., $R = 8$). The closeness between the BCF fragility and necking fragility indicates that the necking-induced failure of the ductile anchor rods governs the failure of the proposed ECBP connection. The collapse fragility of the same SMRF (in black, determined as per Equation (17)) is also plotted in Figure 9A. The much lower collapse fragility than the BCF fragility implies that frame collapse may not occur even if the ECBP connection has failed. As discussed previously in Section 3.2, it may be attributed to the shear integrity that the base connection can maintain after the loss of its flexural capacity. For comparison purposes, Figure 9B depicts all the same fragility curves (as Figure 9A) for the $1.1R_y M_p$ (i.e., strong-base design) case of the 4-story frame. As expected, the BCF fragility is nearly zero along $S_a(T_1)_{GM1}$ in Figure 9B, indicating that the ECBP connection failure is improbable for the strongly-designed base. This is because the plastic hinge is forced into the weaker element (i.e., column bottom end), which may further lead to the sidesway collapse of the frame under higher seismic intensities (see collapse fragility curve in Figure 9B). The fragility curves for the overstrength-designed base (i.e., $\Omega = 3$) case of the 4-story frame are almost
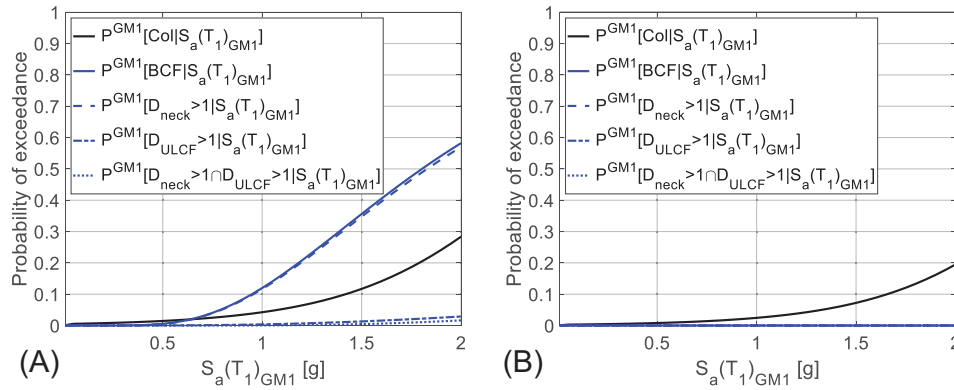
FIGURE 9 Fragility curves of frame collapse, and base connection failure for the 4-story frames subjected to single ground motion (GM1), considering the ECBP connections designed for (A) $R = 8$; and (B) $1.1R_yM_p$ strength levels.
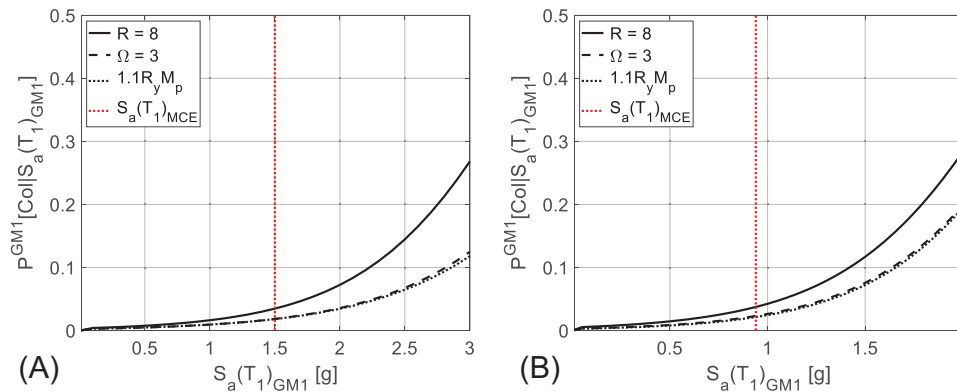

FIGURE 10 Frame collapse fragility curves of (A) 2-story frames; and (B) 4-story frames subjected to single ground motion (GM1), considering the ECBP connections designed for three strength levels.

identical to Figure 9B for the $1.1R_yM_p$ case. This is not unexpected because the difference between capacity-based design and overstrength-based design for 4-story frame bases is modest (see Table 1), such that the ECBP connections designed for $\Omega = 3$ strength are not expected to experience large inelastic rotation (see Figure 6B), and the frame collapse is dominated by the sidesway mechanism. Similar trends regarding the fragility curves subjected to GM1 are observed for the 2-story archetype frames considered in this study.

Figure 10A,B depicts the frame collapse fragilities of the 2- and 4-story archetype SMRFs with ECBP connections designed for three strength levels, respectively. As seen from both panels, the two collapse fragility curves corresponding to the capacity (i.e., $1.1R_yM_p$) and overstrength (i.e., $\Omega = 3$) design approaches for base connections are approximately the same. This is because the design strengths of these two approaches are relatively close for the two considered low-rise frames (see Table 1). Following these design strengths, sidesway collapse may entirely control the seismic performance of the frame, while the inelastic rotations developed in the ECBP connections are limited. On the other hand, the collapse fragility associated with the weak-base design is slightly higher than the rest fragility curves when the seismic intensity (represented by $S_a(T_1)_{GM1}$) is modest, and the difference becomes larger with the $S_a(T_1)_{GM1}$ value increasing. This may be attributed to the flexural failure of the ductile ECBP connections. Even though they can resist the shear demand, the loss of moment capacity results in the shift of the inflection point to the bottom end of the first-story column, finally leading to a soft-story collapse (before the development of the full-building sidesway collapse mechanism).

Table 2 further summarizes the collapse probabilities for both frames corresponding to the three considered base strength levels. These probabilities are obtained directly from the fragility curves of Figure 10 and are evaluated under the 2/50 (i.e., MCE) hazard level (represented as the red dashed lines in Figure 10). Referring to Section 2.1, the corresponding $S_a(T_1)_{MCE}$ values of the 2- and 4-story frames are 1.5 g and 0.94 g, respectively. The collapse probabilities in Table 2 are then compared to the typical acceptance criteria in the guidelines to assess the frame seismic performance. In particular, FEMA P695[58] recommends 10% as the acceptable collapse probability of a frame subjected to ground motions scaled to

TABLE 2 Frame collapse probabilities of 2- and 4-story archetype frames evaluated at the MCE hazard level.

Frame	Strength level $R = 8$	$\Omega = 3$	$1.1R_yM_p$
2-story $[S_a(T_1)_{\text{MCE}} = 1.5\,g]$	3.5%	1.8%	1.8%
4-story $[S_a(T_1)_{\text{MCE}} = 0.94\,g]$	3.7%	2.3%	2.2%
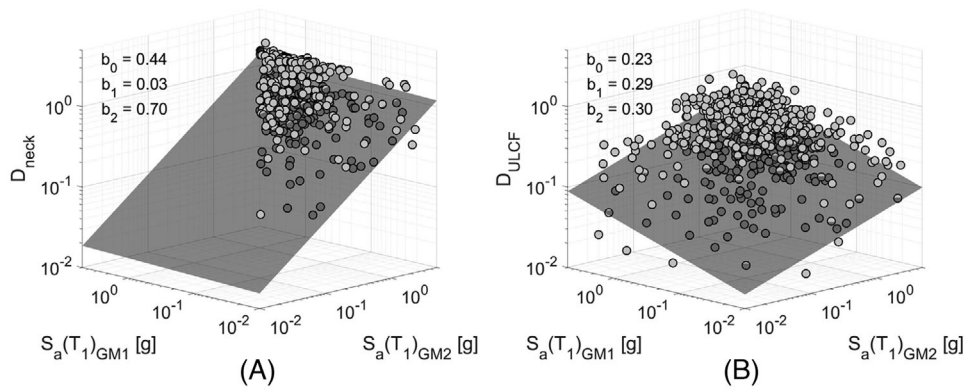
FIGURE 11 Bivariate regression for 2-story frame with $R = 8$ strength level of ECBP connections, considering cloud data of GMS set for (A) D_{neck}; and (B) D_{ULCF}.

the MCE hazard level. According to Table 2, the seismic performance of both SMRFs with base connections designed for $R = 8$ (weak-base design) is acceptable. However, the collapse probabilities for weak-base designed cases are higher than those for the rest design cases. Therefore, designing base connections for $R = 8$ strength level to guarantee acceptable seismic performance requires further investigations. For both considered low-rise frames, design based on overstrength shows similar seismic performance to the capacity-designed cases. It implies that overstrength-based ECBP connection design, allowed by AISC 341-16,[1] has no negative consequence regarding the frame collapse performance.

4.3 | Fragility assessment of SMRFs with ductile ECBPs subject to ground motion sequences

To develop the fragility surface for BCF due to GMS, it is necessary to derive the fragility models of the same frame due to GM2. As an example, Figure 11A,B illustrates the bivariate regressions for D_{neck} and D_{ULCF} of $R = 8$ strength case in the 2-story frame, respectively. As discussed in Section 4.1, only cloud data (conditioned on no BCF due to GM1) showing $S_a(T_1)_{\text{GM1}} < S_a(T_1)_{\text{GM2}}$ is used in Figure 11A. The regression plane and the associated parameters are given in the figure. In Figure 11A for D_{neck}, the fitted exponent of $S_a(T_1)_{\text{GM1}}$ (i.e., b_1) is negligible (close to zero), while the exponent of $S_a(T_1)_{\text{GM2}}$ (i.e., b_2) is significant. This is not surprising because D_{neck} values calculated from GM2 depend mainly on $S_a(T_1)_{\text{GM2}}$. According to Figure 11B, the fitted parameters for both $S_a(T_1)_{\text{GM1}}$ and $S_a(T_1)_{\text{GM2}}$ are close, indicating that the contribution of GM1 to the cumulative damage of D_{ULCF} plays an equal role to the contribution due to GM2 in predicting D_{ULCF} value at the end of GMS.

Figure 12A shows the fragility surface of BCF (given GMS) relating to Figure 11. It is noticed that the fragility curve on the vertical cutting plane for $S_a(T_1)_{\text{GM2}} = 0$ is roughly the same as the BCF fragility due to GM1 only. Then, the BCF probability given $S_a(T_1)_{\text{GM1}}$ further increases due to the presence of GM2 with seismic intensity of $S_a(T_1)_{\text{GM2}}$. This observation may be attributed to the following: (1) for necking fragility estimation, the inelastic strain may exist in the anchor rods due to GM1 and it may further increase during GM2 excitation; and (2) for ULCF fragility estimation, the D_{ULCF} is continuously accumulated if anchor rods reach the inelastic stage due to GM2. Figure 12B shows the BCF fragility surface for the same 2-story frame with base connections designed for $1.1R_yM_p$ strength. Because the ECBP connections are capacity designed, the expected inelastic rotation in the base is still modest, even given two strong ground motions (i.e., GMS). This is confirmed in Figure 12B, as almost no probability of BCF can be observed. A similar BCF fragility surface (to Figure 12B, not shown
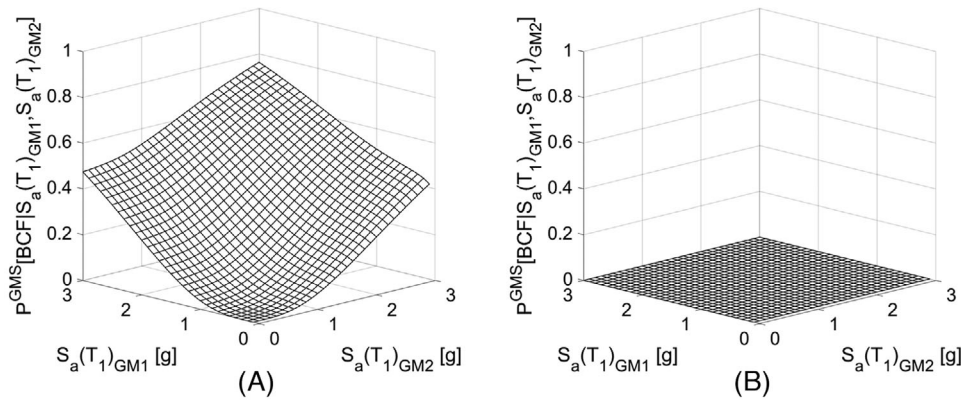
FIGURE 12 Fragility surfaces of base connection failure for the 2-story frames subjected to ground motion sequence of GM1 and GM2, considering the ECBP connections designed for (A) $R = 8$; and (B) $1.1R_yM_p$ strength levels.
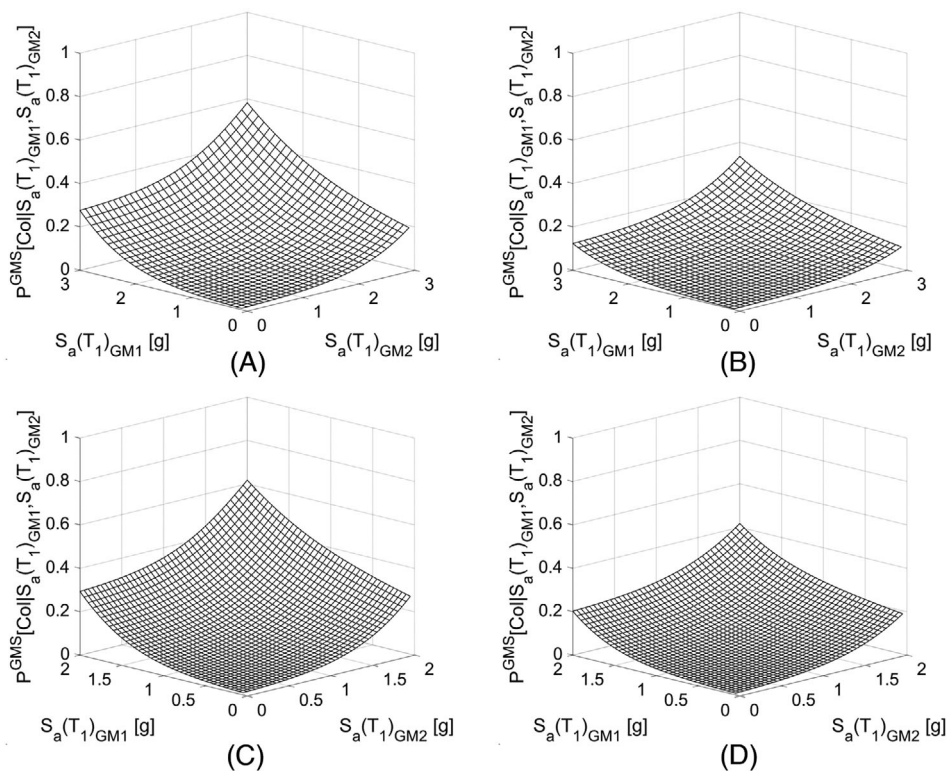

FIGURE 13 Collapse fragility surfaces of 2-story frames with ECBP connections designed for (A) $R = 8$; and (B) $1.1R_yM_p$ strength levels; and 4-story frames with ECBP connections designed for (C) $R = 8$; and (D) $1.1R_yM_p$ strength levels, subjected to ground motion sequence of GM1 and GM2.

for brevity) is also derived for the 2-story frame with overstrength-designed bases. Moreover, these findings also apply to the BCF fragility surfaces (subjected to GMS) for the three 4-story frames considered in this study.

Figure 13 shows the selected collapse fragility surfaces due to GMS (i.e., $P^{\text{GMS}}[\text{Col}|S_a(T_1)_{\text{GM1}}, S_a(T_1)_{\text{GM2}}]$) for both considered frames. The fragility results of $R = 8$ and $1.1R_yM_p$ cases are provided for each frame. Similar to Figure 12, the fragility results given $S_a(T_1)_{\text{GM2}} = 0$ in Figure 13 are the corresponding collapse fragility curves (due to GM1 only) depicted in Figure 10. In each panel of Figure 13, bow-shaped fragility curves along $S_a(T_1)_{\text{GM2}}$ are displayed, given specific $S_a(T_1)_{\text{GM1}}$ values. This is because the considered SMRFs may already have accumulated permanent damage in some elements (due to inelastic responses) under GM1 shaking. A second earthquake (i.e., GM2) can further increase the collapse probability of the unrepaired SMRFs. However, it should be noted that the increase of collapse fragility is modest if the spectral intensity
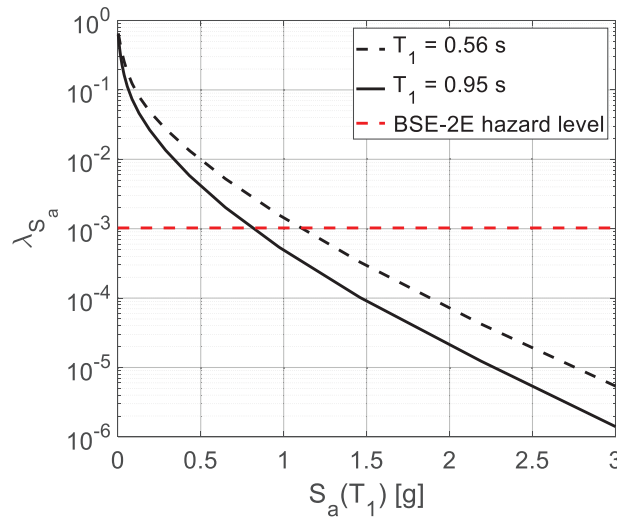
FIGURE 14   Site specific hazard curves for San Jose, California (37.3°N, 121.9°W).

TABLE 3 $S_a(T_1)_{\mathrm{GM1}}$ values [g] of the past seismic event corresponding to 10% collapse probability given $S_a(T_1)_{\mathrm{GM2}}$ of future event = $S_a(T_1)_{\mathrm{BSE\text{-}2E}}$, for considered 2- and 4-story frames.

Frame	Strength level		
	$R = 8$	$\Omega = 3$	$1.1R_yM_p$
2-story [$S_a(T_1)_{\mathrm{BSE\text{-}2E}} = 1.11\,g$]	1.98	2.69	2.68
4-story [$S_a(T_1)_{\mathrm{BSE\text{-}2E}} = 0.82\,g$]	1.13	1.46	1.49

of GM2 (i.e., $S_a(T_1)_{\mathrm{GM2}}$) is low, resulting in relatively flat fragility curves given each $S_a(T_1)_{\mathrm{GM1}}$ value. In addition, a comparison between Figures 12A,B and 13A,B (for the same 2-story frames designed with the same base connection strengths) shows that (1) the collapse fragility of weak-base (i.e., $R = 8$) case is much lower than its BCF fragility; and (2) the collapse fragility of strong-base (i.e., $1.1R_yM_p$) case is controlled entirely by the sidesway collapse without the occurrence of BCF. For each considered frame, the strong-base case exhibits better seismic performance than the weak-base case by showing much lower collapse fragility (see panels A–B or C–D of Figure 13). These findings are consistent with those discussed in Section 4.2 regarding the various BCF and collapse fragility curves derived for GM1 only.

To further quantitatively assess the seismic performance of the considered SMRFs, a simple scenario is investigated—the existing frame has already experienced GM1 with a specific $S_a(T_1)_{\mathrm{GM1}}$ value (i.e., a past seismic event) and remains unrepaired. Then, an independent second ground motion (i.e., GM2, it is a second mainshock or a triggered event) may strike the same frame in the future. As per ASCE 41-17[69] for seismic evaluation of existing buildings, the basic structural performance objective for the investigated frames (with risk category II) under the basic safety earthquake-two for existing buildings (BSE-2E, i.e., 5% probability of exceedance in 50 years, or 5/50 hazard) level is collapse prevention. This damage state indicates that the considered frame is on the threshold of partial or total collapse after an earthquake, and it may not be technically practical to repair.[69] Following the discussion, the unacceptable response of the existing SMRFs (that have survived from GM1) may be defined as the frame collapse given GM2 at BSE-2E hazard level, and a 10% collapse probability measured from the same hazard level is arbitrarily adopted as the acceptable limit (similar to the consideration of FEMA P695[58]).

Since the occurrence of GM2 is independent of the past event (i.e., GM1), the results of the probabilistic seismic hazard analysis (PSHA) for the design site (i.e., San Jose, California: 37.3°N, 121.9°W; and site class D) can be used to determine the 5%-damped spectral acceleration values at BSE-2E hazard level (denoted $S_a(T_1)_{\mathrm{BSE\text{-}2E}}$). Figure 14 shows the PSHA results [i.e., hazard curves—annual rate of exceedance λ_{Sa} versus $S_a(T_1)$] for the two fundamental periods of interest (i.e., $T_1 = 0.56$ s and 0.95 s for the two- and 4-story frames, respectively). The plotted data in Figure 14 is obtained using the Unified Hazard Tool[70] at https://earthquake.usgs.gov/hazards/interactive/, with appropriate interpolation to cover the two periods. The 2008 update of the national seismic hazard maps for the conterminous US[71] is selected. A red dashed line is also plotted in Figure 14 to represent the λ_{Sa} corresponding to the BSE-2E hazard level. The $S_a(T_1)_{\mathrm{BSE\text{-}2E}}$ values for the considered 2- and 4-story frames are 1.11 g and 0.82 g, respectively. Table 3 summarizes the $S_a(T_1)_{\mathrm{GM1}}$ values (of the past

seismic event) for all the considered SMRFs that are associated with 10% collapse probability when GM2 (i.e., the future event) is at BSE-2E hazard level (i.e., $S_a(T_1)_{GM2} = S_a(T_1)_{BSE-2E}$). These values are determined from the corresponding collapse fragility surfaces for GMS (e.g., Figure 13). According to Table 3, both 2- and 4-story frames with weakly-designed ECBP connections show much lower $S_a(T_1)_{GM1}$ values, while the remaining two cases (i.e., $\Omega = 3$ and $1.1R_yM_p$ cases) of each SMRF have similar and larger $S_a(T_1)_{GM1}$ values, indicating much better seismic performance. Nevertheless, all the obtained $S_a(T_1)_{GM1}$ values in Table 3 are much larger than the $S_a(T_1)_{MCE}$ values of the 2- and 4-story frames (i.e., 1.5 g and 0.94 g, respectively). It may be interpreted that the seismic performance of these unrepaired frames subjected to GM2 is acceptable even though the past earthquake (i.e., GM1) that the frames have experienced was stronger than the maximum earthquake set forth in the design standards.[14]

5 | CONCLUSIONS AND LIMITATIONS

This study investigated the effects of the strength of a ductile detail of ECBP connections[13] on the seismic performance of SMRFs. A large suite of NLTHAs of two (2- and 4-story) archetype SMRFs, designed with high seismicity using current design standards, was conducted to achieve this. Given the aims of this study, the ECBP connections of each frame were designed for three levels of strengths; these include (1) the reduced seismic load levels corresponding to $R = 8$; (2) the code-based overstrength seismic loads corresponding to $\Omega = 3$; and (3) the capacity-designed forces corresponding to a moment of $1.1R_yM_p$ of the connected column. These design loads allow the ductile ECBP connections to be strongly or weakly designed, and the corresponding seismic responses of these base connections can vary from elastic to highly inelastic. Frame models for both SMRFs were developed based on currently available simulation practices and component models verified against experiments. Two suites of GMSs, each containing 800 artificially combined records with two ground motions (namely GM1 and GM2), were assembled for cloud-based NLTHAs of both frame models. In addition, fragility assessment of global collapse and BCF subjected to a single ground motion (i.e., GM1) and GMS were performed. In this study, frame sidesway collapse was assumed to occur when the IDR reached 10%, and the BCF was defined as the attainment of one of the two failure modes: necking failure or the ULCF fracture of anchor rods in the ECBP connection. The main findings of the NLTHAs, as well as the fragility analyses, are briefly summarized:

- ECBP connections designed for $R = 8$ strength (i.e., weak-base design) may fail under strong seismic excitation. The governing failure mode is the necking of anchor rods, while the ULCF fracture of anchors is highly unlikely. These weakly-designed base connections show significant rotational ductility (capacity). The achieved base rotations before their necking-induced failure are more than 0.06 rad with very low variability (i.e., CoV $\sim$ 2%).
- For the frames designed with weak bases, global collapse is not observed immediately when the BCF occurs. This is because the base connection can still maintain the shear integrity after the loss of flexural capacity. In addition, it is observed that the first-story mechanism usually controls the collapse of these frames.
- ECBP connections designed for $\Omega = 3$ and $1.1R_yM_p$ (i.e., strong-base design) strength levels only show very limited inelastic rotation during earthquakes. The failure of frames with strong bases is governed by the sidesway collapse, as the inelastic deformations at base levels are enforced to the first-story columns.
- Regarding the fragility curves for the considered SMRFs subjected to GM1 (i.e., single ground motion), the seismic performance of frames with weak bases designed in this study is acceptable. Because their collapse probabilities at the MCE hazard level are much lower than 10%, even though the associated BCF fragilities are relatively high. On the other hand, the BCF fragilities for frames with strong bases are approximately zero, and the corresponding collapse fragilities/probabilities are significantly lower than those for weak-base cases.
- Regarding the fragility surfaces for the assessed SMRFs subjected to GMS (i.e., GM1 followed by GM2), consistent findings from the previous point are obtained. Frames designed with strong bases show better seismic performance than those designed with weak bases. Moreover, the collapse probabilities of all the investigated frames subjected to GM2 may be considered acceptable even if they were not retrofitted after the strike of strong GM1 at the MCE hazard level.

This study has some limitations that must be considered while interpreting its results, for example, for design development. First of all, the current study only designed two SMRFs; for each base design load level, only one ECBP configuration was designed. Although this is useful for assessing the seismic performance of frames with ductile ECBP connections, it may be difficult to generalize the findings because the structural response of some other specific structure and base connection designs may not be similar to those examined in this study. Given the same design parameters/constraints,

multiple design outcomes may be possible. However, this study only took one such design solution for assessment. Secondly, this study utilized a state-of-practice IM (i.e., $S_a(T_1)$ of the code-based fundamental period) to handily interpret results in accordance with design codes. It is important to recognize that the code-based fundamental period is typically lower than the computer-based period for the considered SMRFs,[16] and $S_a(T_1)$ itself may not be an efficient IM for the probabilistic seismic demand analysis.[72] The adoption of code-based $S_a(T_1)$ in this study may slightly affect the accuracy of the seismic performance assessment. Thirdly, bias in the simulation and NLTHAs cannot be discounted. For instance, the axial force-moment interactions in the columns cannot be directly considered in the nonlinear spring hinge-based model (with pre-defined hysteretic rules) utilized in this study (however, the proposed base connection model can capture this effect). The three-dimensional failure modes of the column (e.g., lateral-torsional buckling) were also not simulated in 2D models. Fourthly, the parameters of both damage measures (i.e., D_{neck} and D_{ULCF}) were conservatively selected from the available literature (according to Hassan et al.[13]). This may overestimate the failure probability of the proposed ductile ECBP connections. Moreover, this study did not perform hazard-consistent record selection for GMS sets, and this may affect the fragility results at specific intensity levels of interest (e.g., at the MCE level). Finally, this study focused on the fragility analysis rather than the full seismic risk assessment of the SMRFs, which did not carefully account for the hazard analysis (e.g., probability of occurrence) for both GM1 and GM2. Notwithstanding these limitations, the presented study provides broad insights into the effects of proposed ductile ECBP connections with yielding anchors (designed with a range of strength levels) on the seismic performance of SMRFs.

DATA AVAILABILITY STATEMENT
The data that support the findings of this study are available from the corresponding author upon reasonable request.

ORCID
Ahmad Hassan https://orcid.org/0000-0003-0832-669X
Carmine Galasso https://orcid.org/0000-0001-5445-4911

REFERENCES
1. AISC (American Institute of Steel Construction). *Seismic Provisions for Structural Steel Buildings (ANSI/AISC 341-16)*. American Institute of Steel Construction; 2016.
2. Song B, Galasso C, Kanvinde A. Reliability analysis and design considerations for exposed column base plate connections subjected to flexure and axial compression. *J Struct Eng*. 2021;147(2):04020328. doi:10.1061/(ASCE)ST.1943-541X.0002903
3. Gomez I, Kanvinde A, Deierlein G. *Exposed Column Base Connections Subjected to Axial Compression and Flexure*. American Institute of Steel Construction; 2010.
4. Kanvinde AM, Higgins P, Cooke RJ, Perez J, Higgins J. Column base connections for hollow steel sections: seismic performance and strength models. *J Struct Eng*. 2015;141(7):04014171. doi:10.1061/(asce)st.1943-541x.0001136
5. Trautner CA, Hutchinson T, Grosser PR, Silva JF. Effects of detailing on the cyclic behavior of steel baseplate connections designed to promote anchor yielding. *J Struct Eng*. 2016;142(2):04015117. doi:10.1061/(ASCE)ST.1943-541X.0001361
6. Trautner CA, Hutchinson T, Grosser PR, Silva JF. Investigation of steel column–baseplate connection details incorporating ductile anchors. *J Struct Eng*. 2017;143(8):04017074. doi:10.1061/(ASCE)ST.1943-541X.0001759
7. Falborski T, Torres-Rodas P, Zareian F, Kanvinde A. Effect of Base-connection strength and ductility on the seismic performance of steel moment-resisting frames. *J Struct Eng*. 2020;146(5):04020054. doi:10.1061/(ASCE)ST.1943-541X.0002544
8. Inamasu H, Castro e Sousa A, Güell G, Lignos DG. Anchor-yield exposed column bases for minimizing residual deformations in seismic-resistant steel moment frames. *Earthq Eng Struct Dyn*. 2021;50(4):1083-1100. doi:10.1002/eqe.3392
9. Torres-Rodas P, Flores F, Pozo S, Astudillo BX. Seismic performance of steel moment frames considering the effects of column-base hysteretic behavior and gravity framing system. *Soil Dyn Earthquake Eng*. 2021;144:106654. doi:10.1016/j.soildyn.2021.106654
10. Cravero J, Elkady A, Lignos DG. Experimental evaluation and numerical modeling of wide-flange steel columns subjected to constant and variable axial load coupled with lateral drift demands. *J Struct Eng*. 2020;146(3):04019222. doi:10.1061/(ASCE)ST.1943-541X.0002499
11. Elkady A, Lignos DG. Full-scale testing of deep wide-flange steel columns under multiaxis cyclic loading: loading sequence, boundary effects, and lateral stability bracing force demands. *J Struct Eng*. 2018;144(2):04017189. doi:10.1061/(ASCE)ST.1943-541X.0001937
12. Newell JD, Uang CM. Cyclic behavior of steel wide-flange columns subjected to large drift. *J Struct Eng*. 2008;134(8):1334-1342. doi:10.1061/(ASCE)0733-9445(2008)134:8(1334)

13. Hassan AS, Song B, Galasso C, Kanvinde A. Seismic performance of exposed column–base plate connections with ductile anchor rods. *J Struct Eng.* 2022;148(5):04022028. doi:10.1061/(ASCE)ST.1943-541X.0003298

14. ASCE (American Society of Civil Engineers). *Minimum Design Loads for Buildings and Other Structures (ASCE/SEI 7–10)*. American Society of Civil Engineers; 2010.

15. Jalayer F. *Direct Probabilistic Seismic Anaysis: Implementing Non-linear Dynamic Assessments*. PhD Thesis. Stanford University; 2003.

16. Elkady A, Lignos DG. Effect of gravity framing on the overstrength and collapse capacity of steel frame buildings with perimeter special moment frames. *Earthq Eng Struct Dyn.* 2015;44(8):1289-1307. doi:10.1002/eqe.2519

17. Grilli D, Jones R, Kanvinde A. Seismic performance of embedded column base connections subjected to axial and lateral loads. *J Struct Eng.* 2017;143(5):04017010. doi:10.1061/(ASCE)ST.1943-541X.0001741

18. NEHRP (National Earthquake Hazards Reduction Program). *Evaluation of the FEMA P-695 Methodology for Quantification of Building Seismic Performance Factors, NIST GCR 10-917-8*. National Institute of Standards and Technology, US Department of Commerce; 2010.

19. Medina RA, Krawinkler H. Evaluation of drift demands for the seismic performance assessment of frames. *J Struct Eng.* 2005;131(7):1003-1013. doi:10.1061/(ASCE)0733-9445(2005)131:7(1003)

20. Zareian F, Kanvinde A. Effect of column-base flexibility on the seismic response and safety of steel moment-resisting frames. *Earthquake Spectra.* 2013;29(4):1537-1559. doi:10.1193/030512EQS062M

21. Zareian F, Krawinkler H. Conceptual performance-based seismic design using building-level and story-level decision support system. *Earthq Eng Struct Dyn.* 2012;41(11):1439-1453. doi:10.1002/eqe.2218

22. ASTM (American Society for Testing and Materials). *Standard Specification for Structural Steel Shapes (ASTM A992/A992M-22)*. ASTM; 2022.

23. AISC (American Institute of Steel Construction). *Prequalified Connections for Special and Intermediate Steel Moment Frames for Seismic Applications (AISC 358-16)*. American Institute of Steel Construction; 2016.

24. AISC (American Institute of Steel Construction). *Specification for Structural Steel Buildings (ANSI/AISC 360-16)*. American Institute of Steel Construction; 2016.

25. ACI (American Concrete Institute). *Building Code Requirements for Structural Concrete and Commentary (ACI 318–19)*. American Concrete Institute; 2019.

26. ASTM (American Society for Testing and Materials). *Standard Specification for High-Strength Low-Alloy Columbium-Vanadium Structural Steel (ASTM A572/A572M-18)*. ASTM; 2018.

27. ASTM (American Society for Testing and Materials). *Standard Specification for Anchor Bolts, Steel, 36, 55, and 105-ksi Yield Strength (ASTM F1554-18)*. ASTM; 2018.

28. Fisher JM, Kloiber LA. *Steel Design Guide 1: Base Plate and Anchor Rod Design*. 2nd ed. American Institute of Steel Construction; 2006.

29. Gomez IR. *Behavior and Design of Column Base Connections*. PhD Thesis. University of California; 2010.

30. Torres-Rodas P, Zareian F, Kanvinde A. Seismic demands in column base connections of steel moment frames. *Earthquake Spectra.* 2018;34(3):1383-1403. doi:10.1193/062317EQS127M

31. Mazzoni S, McKenna F, Scott MH, Fenves GL. *Open System for Earthquake Engineering Simulation User Command-Language Manual*. Pacific Earthquake Engineering Research Center, University of California, Berkeley; 2009.

32. Ibarra LF, Medina RA, Krawinkler H. Hysteretic models that incorporate strength and stiffness deterioration. *Earthq Eng Struct Dyn.* 2005;34(12):1489-1511. doi:10.1002/eqe.495

33. Lignos DG, Krawinkler H. Deterioration modeling of steel components in support of collapse prediction of steel moment frames under earthquake loading. *J Struct Eng.* 2011;137(11):1291-1302. doi:10.1061/(ASCE)ST.1943-541X.0000376

34. Lignos DG, Hartloper AR, Elkady A, Deierlein GG, Hamburger R. Proposed updates to the ASCE 41 nonlinear modeling parameters for wide-flange steel columns in support of performance-based seismic engineering. *J Struct Eng.* 2019;145(9):04019083. doi:10.1061/(ASCE)ST.1943-541X.0002353

35. Krawinkler H, Mohasseb S. Effects of panel zone deformations on seismic response. *J Constr Steel Res.* 1987;8:233-250. doi:10.1016/0143-974X(87)90060-5

36. Gupta A, Krawinkler H. *Seismic Demands for Performance Evaluation of Steel Moment Resisting Frame Structures (SAC Task 5.4.3) Technical Report No. 132*. John A. Blume Earthquake Engineering Center, Stanford University; 1999.

37. Torres-Rodas P, Zareian F, Kanvinde A. Hysteretic model for exposed column–base connections. *J Struct Eng.* 2016;142(12):04016137. doi:10.1061/(ASCE)ST.1943-541X.0001602

38. Kent DC, Park R. Flexural members with confined concrete. *J Struct Div.* 1971;97(7):1969-1990. doi:10.1061/JSDEAG.0002957

39. Scott BD, Park R, Priestley MJN. Stress-strain behavior of concrete confined by overlapping hoops at low and high strain rates. *ACI J Proc.* 1982;79(1):13-27. doi:10.14359/10875

40. Gomez IR, Kanvinde AM, Deierlein GG. Experimental investigation of shear transfer in exposed column base connections. *Eng J.* 2011;48(4):245-264.

41. Iervolino I, Giorgio M, Chioccarelli E. Markovian modeling of seismic damage accumulation. *Earthq Eng Struct Dyn.* 2016;45(3):441-461. doi:10.1002/eqe.2668

42. Goda K. Record selection for aftershock incremental dynamic analysis. *Earthq Eng Struct Dyn.* 2015;44(7):1157-1162. doi:10.1002/eqe.2513

43. Goda K, Taylor CA. Effects of aftershocks on peak ductility demand due to strong ground motion records from shallow crustal earthquakes. *Earthq Eng Struct Dyn.* 2012;41(15):2311–2330. doi:10.1002/eqe.2188

44. Ruiz-García J. Mainshock-Aftershock Ground Motion Features and Their Influence in Building's Seismic Response. *J Earthquake Eng.* 2012;16(5):719-737. doi:10.1080/13632469.2012.663154

45. Zhang L, Goda K, De Luca F, De Risi R. Mainshock-aftershock state-dependent fragility curves: a case of wood-frame houses in British Columbia, Canada. *Earthq Eng Struct Dyn*. 2020;49(9):884-903. doi:10.1002/eqe.3269

46. Aljawhari K, Gentile R, Freddi F, Galasso C. Effects of ground-motion sequences on fragility and vulnerability of case-study reinforced concrete frames. *Bull Earthquake Eng*. 2021;19(15):6329-6359. doi:10.1007/s10518-020-01006-8

47. Gentile R, Galasso C. Hysteretic energy-based state-dependent fragility for ground-motion sequences. *Earthq Eng Struct Dyn*. 2021;50(4):1187-1203. doi:10.1002/eqe.3387

48. Bommer JJ, Acevedo AB. The Use of Real Earthquake Accelerograms as Input to Dynamic Analysis. *J Earthquake Eng*. 2004;8(001):43-91. doi:10.1080/13632460409350521

49. Luco N, Bazzurro P. Does amplitude scaling of ground motion records result in biased nonlinear structural drift responses? *Earthq Eng Struct Dyn*. 2007;36(13):1813-1835. doi:10.1002/eqe.695

50. Iacoletti S, Cremen G, Galasso C. Modeling damage accumulation during ground-motion sequences for portfolio seismic loss assessments. *Soil Dyn Earthquake Eng*. 2023;168(2023):107821. doi:10.1016/j.soildyn.2023.107821

51. Ancheta TD, Darragh RB, Stewart JP, et al. NGA-West2 Database. *Earthquake Spectra*. 2014;30(3):989-1005. doi:10.1193/070913EQS197M

52. Bozorgnia Y, Abrahamson NA, Al Atik L, et al. NGA-West2 Research Project. *Earthquake Spectra*. 2014;30(3):973-987. doi:10.1193/072113EQS209

53. Kirkpatrick S, Gelatt CD, Vecchi MP. Optimization by Simulated Annealing. *Science*. 1983;220(4598):671-680. doi:10.1126/science.220.4598.671

54. Xiang Y, Sun D, Fan W, Gong X. Generalized simulated annealing algorithm and its application to the Thomson model. *Phys Lett A*. 1997;233(3):216-220. doi:10.1016/S0375-9601(97)00474-X

55. Dávalos H, Miranda E. Evaluation of the Scaling Factor Bias Influence on the Probability of Collapse Using Sa(T1) as the Intensity Measure. *Earthquake Spectra*. 2019;35(2):679-702. doi:10.1193/011018EQS007M

56. Jalayer F, Ebrahimian H, Miano A, Manfredi G, Sezen H. Analytical fragility assessment using unscaled ground motion records. *Earthq Eng Struct Dyn*. 2017;46(15):2639-2663. doi:10.1002/eqe.2922

57. Pirooz RM, Habashi S, Massumi A. Required time gap between mainshock and aftershock for dynamic analysis of structures. *Bull Earthquake Eng*. 2021;19(6):2643-2670. doi:10.1007/s10518-021-01087-z

58. ATC (Applied Technology Council). *Quantification of Building Seismic Performance Factors (FEMA P695)*. Federal Emergency Management Agency; 2009.

59. Kanvinde AM, Deierlein GG. *Micromechanical Simulation of Earthquake-Induced Fracture in Steel Structures*. John A. Blume Earthquake Engineering Center, Stanford University; 2004. *Technical Report No. 145*.

60. Vian D, Bruneau M. Tests to Structural Collapse of Single Degree of Freedom Frames Subjected to Earthquake Excitations. *J Struct Eng*. 2003;129(12):1676-1685. doi:10.1061/(ASCE)0733-9445(2003)129:12(1676)

61. Vamvatsikos D, Cornell CA. Incremental dynamic analysis. *Earthq Eng Struct Dyn*. 2002;31(3):491-514. doi:10.1002/eqe.141

62. Kanvinde A. Predicting Fracture in Civil Engineering Steel Structures: state of the Art. *J Struct Eng*. 2017;143(3):03116001. doi:10.1061/(ASCE)ST.1943-541X.0001704

63. Smith C, Ziccarelli A, Terashima M, Kanvinde A, Deierlein G. A stress-weighted ductile fracture model for steel subjected to Ultra Low Cycle Fatigue. *Eng Struct*. 2021;245:112964. doi:10.1016/j.engstruct.2021.112964

64. Jalayer F, Ebrahimian H. Seismic risk assessment considering cumulative damage due to aftershocks. *Earthq Eng Struct Dyn*. 2017;46(3):369-389. doi:10.1002/eqe.2792

65. Yu X, Zhou Z, Du W, Lu D. Development of fragility surfaces for reinforced concrete buildings under mainshock-aftershock sequences. *Earthq Eng Struct Dyn*. 2021;50(15):3981-4000. doi:10.1002/eqe.3542

66. Cornell CA, Jalayer F, Hamburger RO, Foutch DA. Probabilistic Basis for 2000 SAC Federal Emergency Management Agency Steel Moment Frame Guidelines. *J Struct Eng*. 2002;128(4):526-533. doi:10.1061/(ASCE)0733-9445(2002)128:4(526)

67. Bakalis K, Vamvatsikos D. Seismic Fragility Functions via Nonlinear Response History Analysis. *J Struct Eng*. 2018;144(10):04018181. doi:10.1061/(ASCE)ST.1943-541X.0002141

68. Bojórquez E, Iervolino I, Reyes-Salazar A, Ruiz SE. Comparing vector-valued intensity measures for fragility analysis of steel frames in the case of narrow-band ground motions. *Eng Struct*. 2012;45(2012):472-480. doi:10.1016/j.engstruct.2012.07.002

69. ASCE (American Society of Civil Engineers). *Seismic Evaluation and Retrofit of Existing Buildings (ASCE/SEI 41-17)*. American Society of Civil Engineers; 2017.

70. USGS (United States Geological Survey). Unified Hazard Tool. Updated June 1, 2022. Accessed January 22, 2023. https://earthquake.usgs.gov/hazards/interactive/

71. Petersen MD, Frankel AD, Harmsen SC, et al. *Documentation for the 2008 update of the United States National Seismic Hazard Maps*. U.S. Geological Survey; 2008. *Open-File Report 2008–1128*.

72. Song B, Galasso C, Kanvinde A. Advancing fracture fragility assessment of pre-Northridge welded column splices. *Earthq Eng Struct Dyn*. 2020;49(2):132-154. doi:10.1002/eqe.3228